TKK Dissertations 124
Espoo 2008

PHOTONIC CRYSTAL WAVEGUIDES FOR SILICON INTEGRATED OPTICS

Doctoral Dissertation

Antti Säynätjoki

Helsinki University of Technology
Faculty of Electronics, Communications and Automation
Department of Micro and Nanosciences

TKK Dissertations 124
Espoo 2008

PHOTONIC CRYSTAL WAVEGUIDES FOR SILICON INTEGRATED OPTICS

Doctoral Dissertation

Antti Säynätjoki

Dissertation for the degree of Doctor of Science in Technology to be presented with due permission of the Faculty of Electronics, Communications and Automation for public examination and debate in Auditorium AS2 at Helsinki University of Technology (Espoo, Finland) on the 23rd of May, 2008, at 12 noon.

Helsinki University of Technology
Faculty of Electronics, Communications and Automation
Department of Micro and Nanosciences

Teknillinen korkeakoulu
Elektroniikan, tietoliikenteen ja automaation tiedekunta
Mikro- ja nanotekniikan laitos

Distribution:
Helsinki University of Technology
Faculty of Electronics, Communications and Automation
Department of Micro and Nanosciences
P.O. Box 3500 (Tietotie 3)
FI - 02015 TKK
FINLAND
URL: http://www.micronova.fi/units/mns/
Tel. +358-9-4511
Fax +358-9-451 3128
E-mail: antti.saynatjoki@tkk.fi

ISBN 978-951-22-9383-4
ISBN 978-951-22-9384-1 (PDF)
ISSN 1795-2239
ISSN 1795-4584 (PDF)
URL: http://lib.tkk.fi/Diss/2008/isbn9789512293841/

TKK-DISS-2476

Multiprint Oy
Espoo 2008

ABSTRACT OF DOCTORAL DISSERTATION	HELSINKI UNIVERSITY OF TECHNOLOGY P. O. BOX 1000, FI-02015 TKK http://www.tkk.fi

Author Antti Säynätjoki

Name of the dissertation

Photonic crystal waveguides for silicon integrated optics

Manuscript submitted 3.3.2008	Manuscript revised 5.5.2008
Date of the defence 23.5.2008	
☐ Monograph	☒ Article dissertation (summary + original articles)

Faculty	Faculty of Electronics, Communications and Automation
Department	Department of Micro and Nanosciences
Field of research	Photonics
Opponent(s)	Prof. Martin Kristensen
Supervisor	Prof. Harri Lipsanen
Instructor	Ph.D. Mikaël Mulot

Abstract

This thesis reports experimental and theoretical studies on photonic crystal waveguides in the silicon-on-insulator platform. The work presents a new variant of Fabry-Pérot method for waveguide characterization. In this method, the reflectivity at the ends of the waveguide under study is enhanced by lithographically patterned mirrors. The thesis also studies a new type of photonic crystal, where the planar photonic crystal lattice is defined with ring-shaped holes (RPhC). By choosing a suitable ring parameter, the RPhC waveguide exhibits low and quasi constant group velocity over a wavelength range of several nanometers. The effect of the modefield width on the dispersion properties of the waveguide is discussed. A short and efficient coupler between the slow mode in an RPhC waveguide and the mode in a conventional silicon waveguide is designed. A relationship between coupling efficiency and the phase match between the coupler mode and the slow mode is observed. These results and observations are important in designing slow-light devices for all-optical signal processing and communication systems. Use of RPhC waveguides in other applications, particularly in biosensing, is also studied. An electron beam writing method that minimizes the writing time of the RPhC lattice is presented. The experimental results on an RPhC waveguide are the first reported for such structure and they show slowdown factors of up to 22 for the group velocity, compared to the group velocity in vacuum.

Keywords Photonic crystals, optical waveguides, photonic integrated circuits, dispersion, silicon-on-insulator	
ISBN (printed) 978-951-22-9383-4	ISSN (printed) 1795-2239
ISBN (pdf) 978-951-22-9384-1	ISSN (pdf) 1795-4584
Language En	Number of pages 62+39
Publisher TKK, Department of Micro and Nanosciences	
Print distribution TKK, Department of Micro and Nanosciences	
☒ The dissertation can be read at http://lib.tkk.fi/Diss/2008/isbn9789512293841/	

VÄITÖSKIRJAN TIIVISTELMÄ	TEKNILLINEN KORKEAKOULU PL 1000, 02015 TKK http://www.tkk.fi

Tekijä Antti Säynätjoki

Väitöskirjan nimi

Photonic crystal waveguides for silicon integrated optics

Käsikirjoituksen päivämäärä 3.3.2008	Korjatun käsikirjoituksen päivämäärä 5.5.2008
Väitöstilaisuuden ajankohta 23.5.2008	
☐ Monografia	☒ Yhdistelmäväitöskirja (yhteenveto + erillisartikkelit)

Tiedekunta	Elektroniikan, tietoliikenteen ja automaation tiedekunta
Laitos	Mikro- ja nanotekniikan laitos
Tutkimusala	Fotoniikka
Vastaväittäjä(t)	Prof. Martin Kristensen
Työn valvoja	Prof. Harri Lipsanen
Työn ohjaaja	Ph.D. Mikaël Mulot

Tiivistelmä

Väitöskirjassa on tutkittu piialustalle valmistettavia planaarisia fotonikidevalokanavia kokeellisesti ja teoreettisesti. Työssä esitetään uusi karakterisointimenetelmä lyhyille fotonikidevalokanaville. Menetelmä perustuu ns. Fabry-Pérot -efektin voimistamiseen tutkittavan valokanavan päihin kuvioitujen peilien avulla. Työssä esitetään myös uudentyyppinen fotonikide, joka muodostetaan renkaanmuotoisista rei'istä. Sopivalla renkaan mitoituksella tämäntyyppiseen fotonikiteseen valmistetussa fotonikidevalokanavassa etenevällä valolla on aallonpituudesta riippumaton ja huomattavan hidas ryhmänopeus (noin c/40) useiden nanometrien aallonpituusvälillä. Pienellä muutoksella renkaan mitoituksessa on suunniteltu rakenne, jonka avulla tämä valokanava voidaan kytkeä tehokkaasti tavanomaisempiin piivalokanaviin. Työssä on havaittu, että muotokentän leveyden aallonpituusriippuvuus vaikuttaa valokanavan dispersio-ominaisuuksiin ja että vaihesovitus vaikuttaa kytkentätehokkuuteen. Nämä tulokset ja havainnot ovat merkittäviä, kun suunnitellaan hidasta valoa soveltavia komponentteja täysoptiseen signaalinkäsittelyyn ja tiedonsiirtojärjestelmiin. Renkaanmuotoisiin reikiin perustuvien fotonikidevalokanavien käyttöä myös muissa sovellutuksissa, erityisesti bioanturina, on tutkittu. Työssä esitellään menetelmä, joka minimoi renkaiden elektronisuihkuvalotukseen kuluvan ajan ja työssä esitetään ensimmäisen kokeelliset tulokset tämäntyyppiseen fotonikiteeseen valmistetusta valokanavasta. Valokanavassa etenevän valon ryhmänopeuden havaittiin hidastuvan 22:nteen osaan valon nopeudesta tyhjössä.

Asiasanat Photonic crystals, optical waveguides, photonic integrated circuits, dispersion, silicon-on-insulator

ISBN (painettu) 978-951-22-9383-4	ISSN (painettu) 1795-2239
ISBN (pdf) 978-951-22-9384-1	ISSN (pdf) 1795-4584
Kieli En	Sivumäärä 62+39

Julkaisija TKK, Mikro- ja nanotekniikan laitos

Painetun väitöskirjan jakelu TKK, Mikro- ja nanotekniikan laitos

☒ Luettavissa verkossa osoitteessa http://lib.tkk.fi/Diss/2008/isbn9789512293841/

Preface

This page is too small to thank everyone I'm grateful to for all the help in making this thesis and all the other research, but here are at least some of the many people I'm indebted to:

I would like to thank Prof. Harri Lipsanen, Prof. Turkka Tuomi (emeritus) and Doc. Markku Sopanen for the opportunity to work on this in this interesting field of science, and for supervision in all the various projects since the first time I entered the Optoelectronics lab nearly ten years ago, Prof. Seppo Honkanen and Doc. Ari Tervonen for providing new view on this study in its last stages,

Dr. Mikaël Mulot, M.Sc. Sanna Arpiainen and Mr. Kevin Vynck for fruitful collaboration in making this thesis, in particular Mikaël for enthusiastically ideating and pushing forward the research, Sanna for sharing her expertise particularly on silicon process technology and Kevin for the discussions on theoretical aspects and for verifying simulation results; VTT Photonics and microfluidics team for letting me use their waveguide characterization setup in our all photonics projects and Dr. Outi Reentilä, Ms. Ying Cui and soon-to-be M.Sc. Amit Khanna for countless hours of assistance with that, M.Sc. Pasi Kostamo for his knowledge on manufacturing anything and M.Sc. Aapo Lankinen for all the never-ending debates on life, the universe and everything,

all my colleagues at Nanotechnology, Photonics and Optoelectronics Groups for helping in all the small and big matters and for creating the great atmosphere in the lab,

lab's Floorball Group for paying their bills sooner or later and for letting me score an easy goal every now and then,

and my friends for trying to keep me away from working on the thesis and, because you can read this book, for eventually failing!

The Finnish Academy, the Finnish Cultural Foundation and the Vaisala Fund are acknowledged for their financial support.

Finally I want to thank my family for their support through all the years of my studies from the first grade up to this point, and my four nieces for giving me breaks from thinking about work - and two of them for occasionally asking me the reminding question "Will your book be finished soon?"...

Antti Säynätjoki Espoo, May 2008

Contents

List of publications

This thesis consists of an overview and of the following publications which are referred to in the text by their Roman numerals.

I A. Säynätjoki, M. Mulot, S. Arpiainen, J. Ahopelto and H. Lipsanen, *Characterization of photonic crystal waveguides using Fabry-Pérot resonances*, J. Opt. A: Pure Appl. Opt. **8**, S502-S506 (2006)

II M. Mulot, A. Säynätjoki, S. Arpiainen, J. Ahopelto and H. Lipsanen, *Slow light propagation in photonic crystal waveguides with ring-shaped holes*, J. Opt. A: Pure Appl. Opt. **9**, S415-S418 (2007)

III A. Säynätjoki, M. Mulot, J. Ahopelto and H. Lipsanen, *Dispersion engineering of photonic crystal waveguides with ring-shaped holes*, Opt. Express **15**, 8323-8328 (2007)

IV A. Säynätjoki, M. Mulot, K. Vynck, D. Cassagne, J. Ahopelto and H. Lipsanen, *Properties, applications and fabrication of photonic crystals with ring-shaped holes in silicon-on-insulator*, Photon. Nanostruct.: Fundam. Applic. **6**, 42-46 (2008)

V A. Säynätjoki, K. Vynck, M. Mulot, D. Cassagne, J. Ahopelto and H. Lipsanen, *Efficient light coupling into a photonic crystal waveguide with flatband slow mode*, Photon. Nanostruct.: Fundam. Applic., in press, doi:10.1016/j.photonics.2008.03.001

Author's contribution

The author has written the manuscripts for publications I, III, IV and V and contributed in the writing of manuscript II. The design work in all the papers and optical characterization in papers I and II has been mainly carried out by the author and M. Mulot, and the sample processing for papers I and II has been mainly carried out by M. Mulot and S. Arpiainen. The author has been the main contributor in the design work in papers III and V and in the analysis in papers I, III and V. Except for the simulation of Fig. 5.9, which was made by K. Vynck, all the simulations in the thesis have been carried out by the author.

1 Introduction

Optical technology is used in many applications. For example, optical communication networks have enabled the development of the Internet, where the bandwidth demand is increasing constantly. This evolution is driven by the increasing number of users, higher subscriber connection bandwidths and the introduction of new bandwidth-greedy services by the service providers. The capacity of the communication systems is not limited by the optical bandwidth but by the speed of the electronic signal processing. All-optical devices, i.e., devices where no conversion between optical and electrical signals is required, open the way to faster signal processing.

Silicon has become the dominating material of microelectronics for various reasons: in addition to its suitable electronic properties, its natural oxide is stable and can easily be used as an electrical insulator. It can also be extracted from sand, literally [1], which makes it cost-effective and the material source practically inexhaustible. Silicon is also a desired material for integration of optics [2–4]. Silicon is transparent above the wavelength of 1200 nm, which is convenient in communications systems, where single mode fibers used in long haul signal transmission operate at wavelengths around 1300 nm and 1550 nm. *Silicon photonics* benefits from the mature processing technology of microelectronics. The silicon-on-insulator (SOI) substrate, while being developed for the microelectronics, is a good substrate for optical integration. The SOI structure, shown schematically in Fig. 1.1a, constitutes a *slab waveguide*, where propagating light can be confined into the device layer, which has a higher refractive index than the underlying buried oxide layer. A laterally confining structure, such as the *strip waveguide* (SW) in Fig. 1.1b, can be fabricated by patterning the device layer. The high refractive index contrast between the surrounding materials and silicon in the strip waveguide makes it possible to confine light into sub-micron cross-sectional dimensions. Strip waveguides also enable micrometer-sized bends and thereby ultra-compact ring-resonators [3, 5]. Using the free-carrier effects in silicon [6, 7], modulators have been realized using high-index-contrast silicon waveguides [5, 8–10].

Non-linear effects are invoked in the tightly confined optical field at sub-milliwatt power levels [11, 12] and all-optical silicon devices such as a Raman laser [13], wavelength converter [14], signal regenerator [15] and logic gates [16] have been demonstrated. Some of the devices are capable of modulation frequencies up to

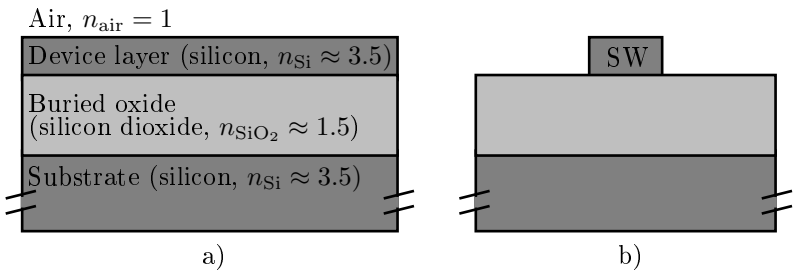

Figure 1.1. Schematic cross-sectional images of a) the silicon-on-insulator (SOI) substrate, b) strip waveguide (SW) manufactured into the SOI substrate by etching. The strip waveguide may be capped with e.g. silicon dioxide.

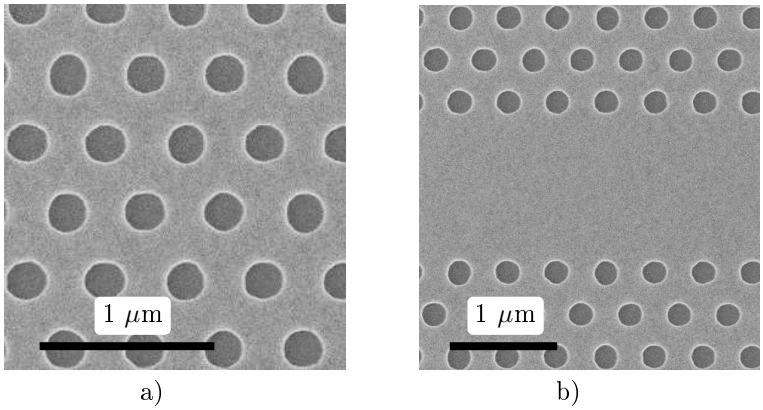

Figure 1.2. Scanning electron micrograph of a) 2D photonic crystal lattice manufactured into the SOI substrate, b) waveguide defined by 3 missing rows in the PhC lattice (Paper I).

40 GHz [9, 14] and have dimensions in the order of 10 μm [5, 9, 16], showing the potential of silicon-based photonic circuits. However, the length of an all-optical device may be several centimeters [14], and miniaturization of the devices would enable larger scale integration and reduction of their operating power. Periodic structures called photonic crystals (PhCs) are foreseen to provide means for denser optical integration.

Figure 1.2a shows a *planar PhC*, which is manufactured by etching a 2D periodic lattice of holes into the SOI structure. The periodic structure diffracts light, and an interference pattern is generated into the structure. For a certain range of frequencies, called the *photonic bandgap*, the interference is destructive regardless of the propagation direction in the plane.

The planar PhC can be manufactured by patterning a slab waveguide with a lithographic technique. Most of the research work is carried out employing electron beam lithography (EBL), which is well suitable for manufacturing prototypes. Large scale production capable patterning of PhCs has been demonstrated using deep-UV

lithography [17, 18] and nanoimprint lithography [19]. After defining the pattern, it is transferred into the slab waveguide usually by using plasma etching.

The planar PhC itself can be utilized e.g. as a mirror [20], collimator [21, 22] or superprism [23]. Defects such as the missing rows of holes in Fig. 1.2b give rise to local states, which can act e.g. as waveguides or high-Q cavities [24, 25]. The PhC waveguide (PhCW) can be coupled with conventional strip waveguides, and SOI-based devices such as wavelength multiplexers/demultiplexers based on this technique have been demonstrated [26, 27]. The PhCW exhibits low group velocity at certain frequencies due to its periodic boundaries [25, 28–32], which makes it possible to realize ultra-compact active photonics devices [33]. In the nonlinear applications, the reduced group velocity increases the intensity of the optical field and therefore enhances nonlinearities [32, 34–37]. Slow-light waveguides may thus reduce the footprint of the nonlinear photonic devices by more than the slowdown factor [34], and also lower the optical power required in the nonlinear processes.

In order to be useful in telecommunications or signal processing applications, the slow-light devices must transmit signals efficiently and with little deterioration. The slow modes have typically a high group velocity dispersion (GVD), which leads to pulse deformation. Therefore it is important to design slow-light structures with tailored dispersion properties. Coupling into the slow modes is not trivial either, due to modefield and impedance mismatch. PhCWs have overcome both these challenges, as slow-light PhCWs with low GVD [38–40] and efficient and compact couplers with conventional strip waveguides [32, 41–44] have been presented.

The main focus in this thesis is in the design and characterization of line defect waveguides in SOI based planar photonic crystals. In Chapters 2 and 3, basic theory of integrated optics and photonic crystals is presented. Chapter 4 describes the equipment and basic techniques used in the fabrication and characterization of the samples in the thesis and presents a new characterization method of short PhC waveguides. This variant of the Fabry-Pérot (F-P) method utilizes the normally troublesome reflections generated at the chip ends.

Chapter 5 presents a new geometry of photonic crystal, consisting of ring-shaped (i.e., annular) holes (RPhC). The peculiar properties of the RPhC are utilized to minimize the GVD of the slow mode in the RPhC waveguide and to realize an efficient coupler into such mode. The dispersion tailored structure also reveals new information on the slow-light coupling in PhCWs. Other potential applications of the RPhC waveguides, such as biosensing, are also discussed in Chapter 5. Finally, the first experimental results on RPhC waveguides are shown.

2 Fundamental concepts

This Chapter presents some theoretical concepts that are essential in designing and understanding the photonic devices in this thesis. The master equations, on which all the theory is built, will be presented first. The equations are applied to describe the propagation of light in homogeneous media and in the SOI structure. The computational methods used in this work are described.

2.1 Master equation

The electric field $\mathbf{E}$, magnetic field $\mathbf{H}$ and charge density ρ are functions of the space coordinate vector $\mathbf{r}$ and time t and connected to each other by the Maxwell's equations

$$\nabla \times \mathbf{E} = -\frac{\partial}{\partial t}(\mu \mathbf{H}) \tag{2.1}$$

$$\nabla \times \mathbf{H} = \frac{\partial}{\partial t}(\epsilon \mathbf{E}) + \sigma \mathbf{E} \tag{2.2}$$

$$\nabla \cdot (\epsilon \mathbf{E}) = \rho \tag{2.3}$$

$$\nabla \cdot (\mu \mathbf{H}) = 0. \tag{2.4}$$

In an isotropic medium, the permittivity $\epsilon(\mathbf{r})$, permeability $\mu(\mathbf{r})$ and the microscopic electric conductivity $\sigma(\mathbf{r})$ of the medium are scalar. The permittivity is usually written as $\epsilon = \epsilon_0 \epsilon_r$, where ϵ_0 is the permittivity of vacuum and $\epsilon_r(\mathbf{r})$ is the relative permittivity of the material. The materials in this work can be considered as non-magnetic insulators, i.e. $\mu = \mu_0$ and $\sigma(\mathbf{r}) = 0$. Therefore, the material is defined by its permittivity distribution $\epsilon_r(\mathbf{r})$, and Eqs. 2.1 and 2.2 are

$$\nabla \times \mathbf{E}(\mathbf{r}, t) = -\frac{\partial}{\partial t}[\mu_0 \mathbf{H}(\mathbf{r}, t)] \tag{2.5}$$

$$\nabla \times \mathbf{H}(\mathbf{r}, t) = \frac{\partial}{\partial t}[\epsilon_0 \epsilon_r(\mathbf{r}) \mathbf{E}(\mathbf{r}, t)]. \tag{2.6}$$

Solving Eq. 2.6 for $\mathbf{E}$ and inserting it into the time derivative of Eq. 2.5 yields

$$\nabla \times \left(\frac{1}{\epsilon_0 \epsilon_r(\mathbf{r})} \nabla \times \mathbf{H}(\mathbf{r}, t) \right) = -\frac{\partial^2}{\partial t^2} \mu_0 \mathbf{H}(\mathbf{r}, t). \tag{2.7}$$

Assuming harmonic time dependence for the magnetic field with (angular) frequency ω, $\mathbf{H}(\mathbf{r}, t) = \mathbf{H}(\mathbf{r}) e^{-i\omega t}$, Eq. 2.7 can thus be written in *frequency domain* as

$$\nabla \times \left(\frac{1}{\epsilon_r(\mathbf{r})} \nabla \times \mathbf{H}(\mathbf{r}) \right) = \left(\frac{\omega}{c} \right)^2 \mathbf{H}(\mathbf{r}), \tag{2.8}$$

where $c = 1/\sqrt{\epsilon_0 \mu_0}$ is the speed of light in vacuum. Eq. 2.8 is known as the *master equation* for the magnetic field.

2.2 Propagation of light

In a homogeneous material, Eq. 2.8 can be written as [1]

$$\nabla^2 \mathbf{H}(\mathbf{r}) = -n^2 \left(\frac{\omega}{c} \right)^2 \mathbf{H}(\mathbf{r}), \tag{2.9}$$

where $n = \sqrt{\epsilon_r}$ is the *refractive index* of the material. The same equation can be derived for the electric field. The general solution to Eq. 2.9 is a superposition of plane waves of the form

$$\mathbf{H}(\mathbf{r}, t) = \mathbf{H}_0 e^{i\mathbf{k}\cdot\mathbf{r}} e^{-i\omega t}, \tag{2.10}$$

where $k = |\mathbf{k}| = n\frac{\omega}{c} = n\frac{2\pi}{\lambda}$, where λ is the vacuum wavelength; $\omega = 2\pi f = 2\pi \frac{c}{\lambda}$. Eq. 2.10 describes a plane wave traveling into a direction defined by $\mathbf{k}$ at the *phase velocity* v_p

$$v_\mathrm{p} = \frac{\omega}{k} = \frac{c}{n}. \tag{2.11}$$

The phase velocity v_p gives the velocity of propagation of a monochromatic wavefront. However, in signal transmission the light is modulated by e.g. varying the intensity or phase of the electromagnetic field. The modulated light is no more monochromatic, and the modulation pattern propagates at the *group velocity* v_g

$$v_\mathrm{g} = \frac{\partial \omega}{\partial k} = \frac{c}{n_\mathrm{g}}. \tag{2.12}$$

where n_g is the *group index*. In the theoretical case of a constant n, $v_\mathrm{p} = v_\mathrm{g} = \frac{c}{n}$. However, n generally depends on ω, therefore the *dispersion relation* $\omega(\mathbf{k})$ is not

[1] $\nabla \times \nabla \times \mathbf{H} = \nabla(\nabla \cdot \mathbf{H}) - \nabla^2 \mathbf{H} = -\nabla^2 \mathbf{H}$.

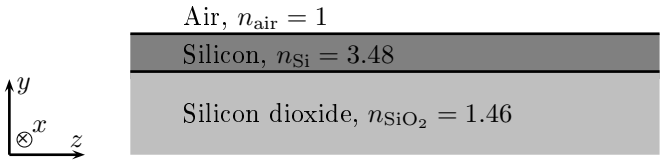

Figure 2.1. Schematic of an SOI waveguide and the coordinates used throughout this thesis. The slab is oriented in the xz plane, and the light propagates into the z direction. The refractive index values are given for the wavelength 1550 nm.

perfectly linear and $v_{\mathrm{g}} \neq v_{\mathrm{p}}$.

2.3 Optical confinement in silicon-on-insulator

Let us consider an SOI structure where the layers are in the xz plane and infinite (Fig. 2.1). An electromagnetic plane wave propagating into the z direction with a *propagation constant* β is described with a function

$$\mathbf{H}(y, z, t) = \mathbf{H}(y)e^{i\beta z}e^{-i\omega t}. \tag{2.13}$$

Eq. 2.9 can be applied in each layer of the structure to obtain

$$\frac{\partial^2}{\partial y^2}\mathbf{H}(y) = \left[\beta^2 - n_{\mathrm{i}}^2\left(\frac{\omega}{c}\right)^2\right]\mathbf{H}(y) = k_{y,\mathrm{i}}^2\mathbf{H}(y), \tag{2.14}$$

where $k_{y,\mathrm{i}}^2 = \beta^2 - n_{\mathrm{i}}^2\left(\frac{\omega}{c}\right)^2$ and n_{i} is the refractive index of one of the three layers. Eq. 2.14 has a general solution

$$\mathbf{H}(y) = \mathbf{H}_{0+}e^{k_{y,\mathrm{i}}\cdot(y+y_{0,\mathrm{i}+})} + \mathbf{H}_{0-}e^{-k_{y,\mathrm{i}}\cdot(y+y_{0,\mathrm{i}-})}, \tag{2.15}$$

which is a combination of exponential functions when $k_{y,\mathrm{i}}$ is real, i.e. when $\beta > n_{\mathrm{i}}\frac{\omega}{c}$. When $n_{\mathrm{i}}\frac{\omega}{c} > \beta$, Eq. 2.15 is a sinusoidal function. Non-zero and limited solution to Eq. 2.8 is obtained when the field is sinusoidal in silicon and exponentially decaying in the air and in the oxide, i.e., when $n_{\mathrm{SiO_2}}\frac{\omega}{c} < \beta < n_{\mathrm{Si}}\frac{\omega}{c}$. The optical wave satisfying this condition is guided in the silicon slab.

The partial solutions must be connected in such a way that Eq. 2.8 is valid in the interfaces in the structure. This yields *interface conditions*, which depend on the direction of the electric and magnetic field vectors, i.e. on the *polarization* of the field. The field must therefore be split into two components: for one, **E** vector is in the xz plane, and for the other, **H** vector is in the xz plane. These components are

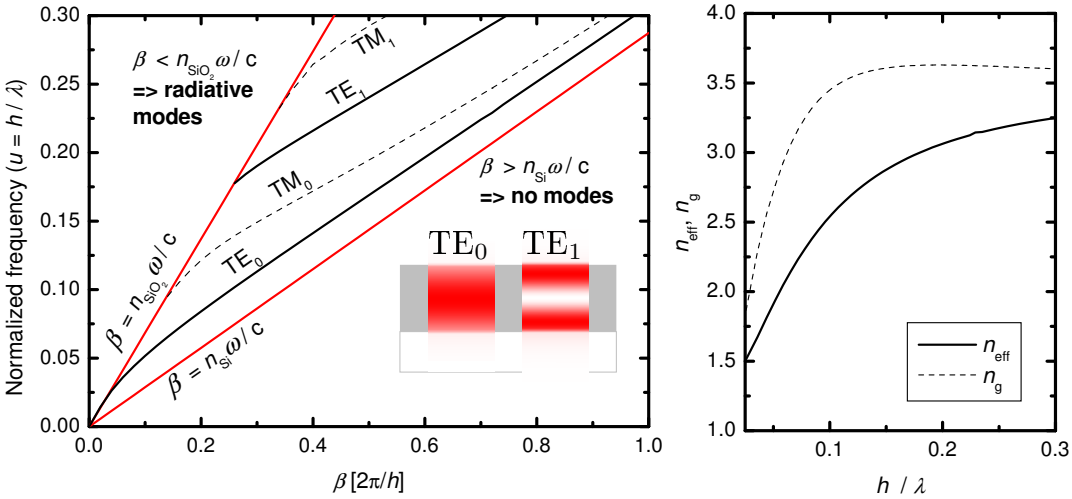

Figure 2.2. a) Dispersion relation of the guided modes in silicon-on-insulator (solid lines: TE modes, dashed lines: TM modes). The inset illustrates electric field energy density distribution in TE_0 and TE_1 modes, b) Effective index n_{eff} and group index n_{g} of the fundamental TE mode as a function of h/λ, where h is the silicon layer thickness and λ is the wavelength.

called TE and TM polarizations, respectively.

Figure 2.2a shows the dispersion relation $\omega(\beta)$ of the modes in the SOI structure with silicon thickness h. The frequency and propagation constant are given in units $[\omega] = 2\pi c/h$ and $[\beta] = 2\pi/h$. With ω and β in these units, the effective (refractive) index $n_{\mathrm{eff}} = \beta/\omega$ and $n_{\mathrm{g}} = (\partial\omega/\partial\beta)^{-1}$. Converting the frequency into a dimensionless quantity yields the *normalized frequency* $u = \omega \cdot \frac{h}{2\pi c} = \frac{h}{\lambda}$.

The effective and group index of the TE_0 mode in the silicon slab are plotted into Fig. 2.2b as a function of h/λ. The effective index increases with increasing frequency because a larger part of the mode is confined into silicon at higher frequencies. Due to this *waveguide dispersion*, $n_{\mathrm{g}} \neq n_{\mathrm{eff}}$ even with the unnatural assumption of frequency independent n.

2.3.1 Effective index approximation

When designing planar photonic structures, the *effective index approximation* is often used, i.e., the vertical structure is replaced with the effective index of a guided mode in it. In this way, the 3D problem is reduced into two dimensions and the computational effort needed in the design is significantly reduced.

With the effective index approximation, the effects of the vertical dimension need to be considered separately. Coupling to radiative modes occurs when $\beta < n_{\mathrm{SiO_2}}\frac{\omega}{c}$, i.e.

when the mode is above the *light line* of the cladding in the dispersion relation plot. The vertical structure exhibits waveguide dispersion, which may shift the frequencies of the modes. The waveguides patterned into a non-symmetrical slab such as the SOI structure no longer possess pure TE and TM polarized modes but quasi TE and TM modes, which may be coupled. All these effects are potentially significant and they will be discussed later in this thesis.

2.4 Computational methods

2.4.1 Finite difference time domain method

Solving the equations 2.1 and 2.2 for the time derivatives yields a set of differential equations. To obtain numerical solutions for these equations, the structure and the electromagnetic field can be discretized into a mesh of nodes. After introducing a known initial field and sources into the computational domain, time development of the field in the structure can be calculated in discrete time steps [45]. This *finite difference time domain* (FDTD) method is therefore best suitable for modeling time-dependent problems, e.g. simulating pulse propagation through a photonic device. The spectral response of the device can be deduced from the time evolution of the field using the Fourier transform.

The FDTD method solves the Maxwell's equations without any assumptions, therefore it is flexible in terms of the geometry of the device under study. However, a dense discretization grid is needed in order to achieve good accuracy[2], therefore FDTD simulations are memory and time consuming.

The FDTD simulations in this work have been carried out using a freely available software [46]. The software solves the electromagnetic field in 2D only, therefore the effective index approximation must be applied. On the other hand, using the 2D grid saves a lot of memory, which makes it possible to carry out FDTD simulations with a normal desktop or laptop computer.

[2]The spatial grid must naturally be dense enough so that the change of the field between the grid points is nearly linear. Moreover, to obtain numerical stability, the time step Δt must fulfill the criterion $\Delta t < \frac{1}{c\sqrt{\frac{1}{\Delta x^2}+\frac{1}{\Delta y^2}+\frac{1}{\Delta z^2}}}$, where c is the speed of light in the material where it is highest in the computational domain and Δx, Δy and Δz are the spatial discretization step sizes.

2.4.2 Plane wave expansion method

According to Bloch theorem, $\mathbf{H}$ (and similarly $\mathbf{E}$) in a periodic structure can be expressed as a superposition of waves $\sum_{\mathbf{k}} \mathbf{H}_{\mathbf{k}}$, where

$$\mathbf{H}_{\mathbf{k}} = e^{i\mathbf{k}\cdot\mathbf{r}}\mathbf{u}_{\mathbf{k}}(\mathbf{r}), \tag{2.16}$$

i.e., plane waves modulated by a periodic function, where $\mathbf{u}_{\mathbf{k}}(\mathbf{r})$ has the same periodicity as the structure. By substituting the periodic functions $\epsilon_r(\mathbf{r})$ and $\mathbf{u}_{\mathbf{k}}(\mathbf{r})$ by their Fourier series, the differential equation 2.8 can be converted into an algebraic eigenvalue problem, which can be solved numerically. As a result one obtains a set of eigenvalues ω/c for each $\mathbf{k}$: the optical modes are solved in the wave vector space, i.e., the *reciprocal space*.

The dispersion relations in this work have been calculated using the MIT Photonic Bands software [47]. The structures in these planewave expansion (PWE) simulations are necessarily perfectly periodic. However, some structures with no perfect periodicity, such as cavities and straight waveguides, can be simulated by implementing a supercell [48].

3 Planar photonic crystals

Photonic bandgaps in periodic media are discussed. First, the formation of bandgaps in 1D periodic media is shown. Subsequently, the two-dimensionally periodic lattice used in this work is presented. Finally, the guided modes in line defects in photonic crystals are discussed.

3.1 1D periodic media

Figure 3.1 shows a 1D periodic stack of high and low refractive index layers. The period of the structure is a. Consider an optical wave propagating perpendicularly to the interfaces, defined as the z direction in Fig. 3.1.

Figure 3.2 shows the dispersion relation[3] of the structure shown in Fig. 3.1 with $n_0 = 2.5$, and with Δn values of 0.2, 1 and 2. Near $k_z = 0$, the dispersion relation is nearly linear, corresponding to $n_\mathrm{g} = 2.5$. With increasing k_z, the slope of the dispersion curves get smaller and vanishes at $k_z = \pi/a$. This has two significant consequences: first, for certain ranges of frequencies there is no propagating mode; photonic bandgaps are formed. Second, as the group velocity is defined as the slope of the dispersion curve, v_g vanishes at the bandgap. As can be seen in Fig. 3.2, the bandgap is wider at larger Δn.

The dispersion relation is periodic with a period $2\pi/a$ and mirror symmetric with respect to the point π/a. Therefore it is adequate to study the modes within the wave number interval $k_z \in [0, \pi/a]$, which is called the *first Brillouin zone* of the *reciprocal lattice* of the periodic structure.

The 1D photonic crystal is a good example structure to theoretically show the origin of the bandgap. It also has many applications e.g. as a laser mirror in vertical cavity surface emitting lasers [49] and as a fiber Bragg grating, which can also act as a laser mirror, or e.g. as a dispersion compensator or a wavelength filter [50]. However, more functionality can be achieved with 2D photonic crystals, which can be used e.g.

[3] In the rest of this thesis, the lattice period a is the length unit used in the normalization of ω and β.

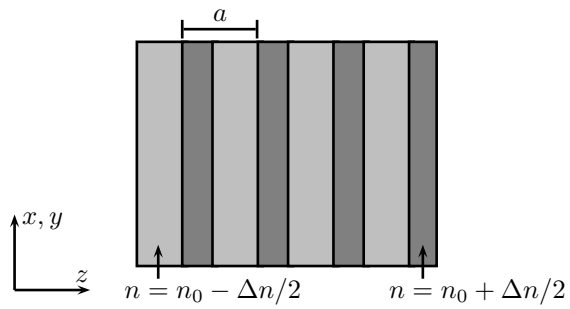

Figure 3.1. Schematic of a 1D periodic structure.

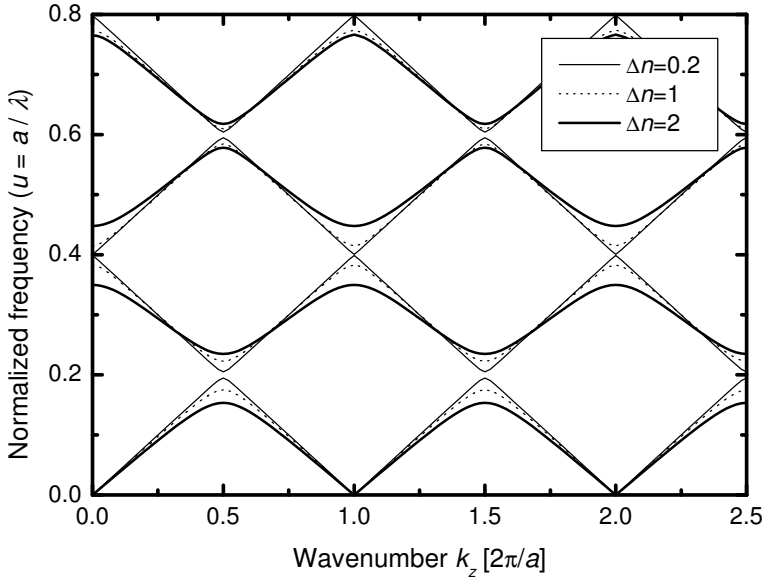

Figure 3.2. Dispersion relation of the structure in Fig. 3.1 with $n_0 = 2.5$.

for guiding light along the plane. The 1D periodic bandgap can be generalized into higher dimensions if the frequency range is forbidden regardless of the propagation direction. This is possible if the refractive index contrast is large and the lattice has a high order of rotational symmetry.

3.2 2D periodic media

The triangular lattice shown in Fig. 3.3a has the highest possible order of rotational symmetry (6-fold symmetry) for a 2D lattice. It is usually realized by etching round holes (radius R) into a dielectric. The separation of the holes is the *lattice constant* a, as shown in Fig. 3.3a. The *air-fill factor* f_{air} of the lattice, i.e. the fraction of air

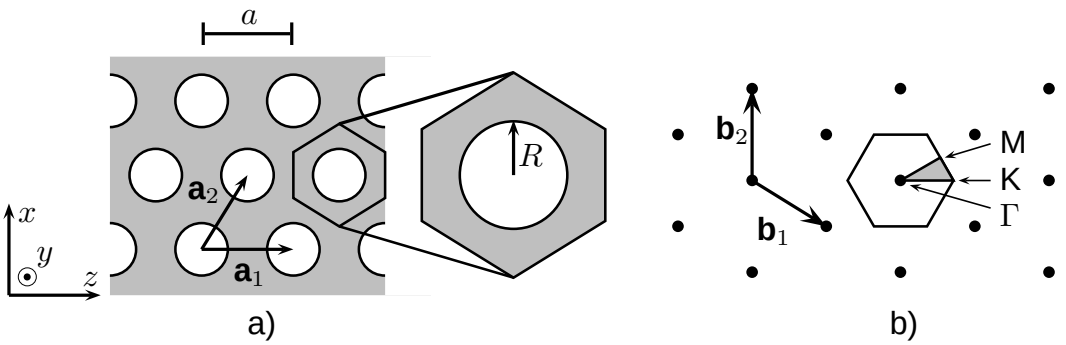

Figure 3.3. a) Schematic of a triangular lattice introducing parameters a and R and lattice vectors $\mathbf{a}_1$ and $\mathbf{a}_2$, b) its reciprocal lattice with reciprocal lattice vectors $\mathbf{b}_1$ and $\mathbf{b}_2$. The hexagon is the first Brillouin zone and Γ, K and M are its high symmetry points. The gray triangle is the reduced Brillouin zone.

in the structure, is

$$f_{\text{air}} = \frac{2\pi}{\sqrt{3}a^2} R^2. \tag{3.1}$$

The reciprocal lattice of the triangular lattice is also triangular (Fig. 3.3b) and its first Brillouin zone is a hexagon. The symmetry allows to limit the $\mathbf{k}$ space under study to the reduced Brillouin zone, which is shown in gray in Fig. 3.3b. The dispersion relation $\omega(\mathbf{k})$ is a 2D surface, which is difficult to study quantitatively. Therefore, ω is plotted only as a function of wave vectors at the edges of the reduced Brillouin zone, i.e., along the path between the Γ, K and M points.

Most of the calculations in this work are made as 2D calculations using the effective index approximation. In the purely two-dimensional picture, the electromagnetic field can be divided into two orthogonal polarizations. Using the same convention as in Section 2.3, the TE (TM) polarization has its electric (magnetic) field in the xz plane.

The focus in the thesis is on SOI based PhCs, therefore the dielectric in consideration is a silicon slab on silicon dioxide. The asymmetric slab makes the polarizations in SOI based 2D PhCs theoretically non-separable, but it has little effect on the actual modes [51]. The SOI based PhC can also be made vertically symmetric either by etching the underlying oxide away, or by growth or bonding of SiO_2 onto the chip.

Figure 3.4 shows the dispersion relation of three lowest-frequency TE polarized modes in a triangular lattice of air holes ($n_{\text{air}} = 1$) with radius $R = 0.3a$ in a dielectric with $n_{\text{eff}} = 2.81$, which corresponds to the effective index of the SOI

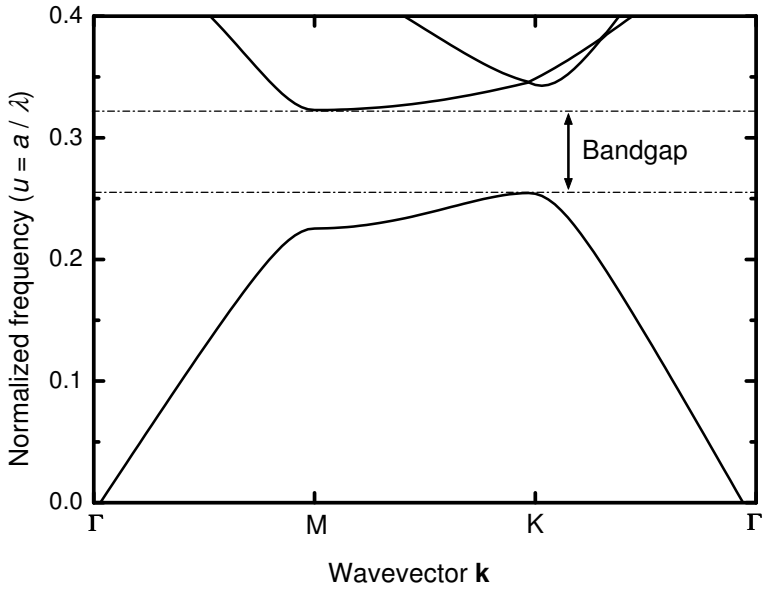

Figure 3.4. Band structure for the TE polarized light in the triangular lattice of air holes with $R = 0.3a$ in a material with $n_{\text{eff}} = 2.81$.

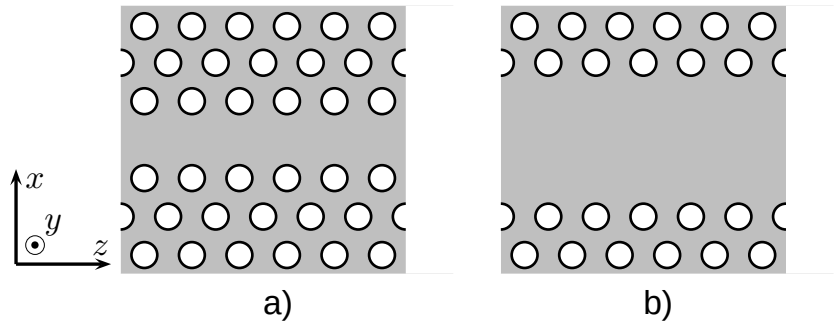

Figure 3.5. Schematic of line defect waveguides in the triangular 2D photonic crystal lattice. a) W1 waveguide, b) W3 waveguide.

structure with a 240 nm thick silicon layer. A bandgap is seen between about $a/\lambda = 0.255$ and $a/\lambda = 0.32$.

3.3 Photonic crystal waveguides

Figure 3.5 shows schematics of two line defect waveguides in the 2D PhC lattice of Fig. 3.3a. The Wn waveguide is formed by omitting n rows of holes in the lattice; Figs. 3.5a and b show a W1 waveguide and a W3 waveguide, respectively.

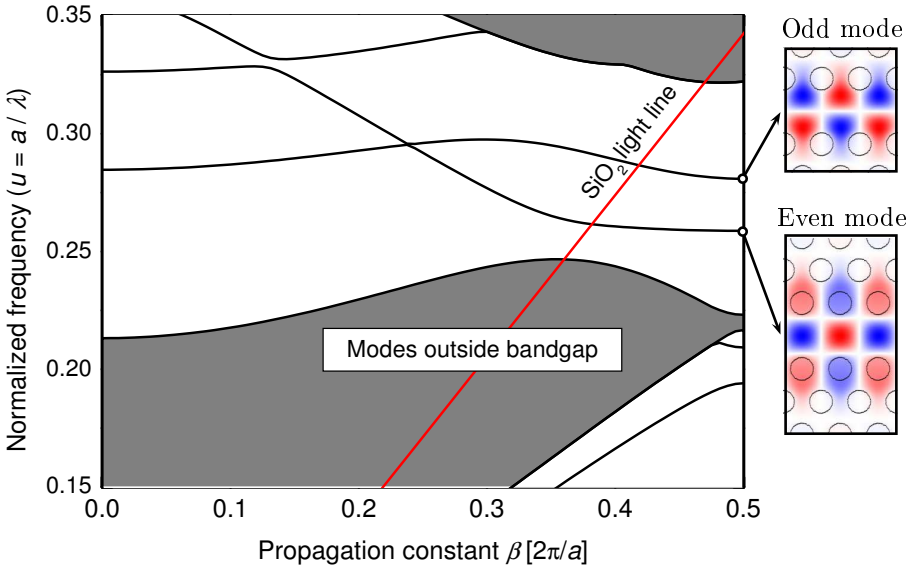

Figure 3.6. Band structure of the TE modes in a W1 waveguide in the triangular lattice of air holes with $R = 0.3a$ and $n_{\text{eff}} = 2.81$. Distribution of the magnetic field perpendicular to the lattice plane, H_y, of the two bandgap guided modes at $\beta = \pi/a$ is shown on the right.

3.3.1 Modes in the W1 waveguide

Figure 3.6 shows the band structure of the TE polarized modes in a W1 waveguide in the lattice with $R = 0.3a$ in a material with $n_{\text{eff}} = 2.81$. The waveguide supports two modes within the bandgap: one with an even parity and one with an odd parity.

The light line of SiO_2 is drawn into Fig. 3.6. Below the light line, the waveguide mode in an SOI based PhC waveguide is theoretically lossless. Oxide-clad waveguides with losses in the order of 1.5 dB/mm for such modes have been realized [18, 25]. Above the light line, the mode is coupled to the oxide cladding due to the periodicity, and losses in the order of 100 dB/mm have been observed for the modes in this regime (see e.g. [52, 53]).

The mode labeled as "Even mode" in the dispersion diagram of Fig. 3.6 is the fundamental mode of the waveguide. It is the mode of practical interest because it is best coupled to the usually single-moded photonic circuits. Two regions with different characteristics are seen in its dispersion curve:

- At small β, the slope of the dispersion curve is nearly constant and it corresponds to $v_g \approx c/n_{\text{eff}}$. This is a characteristic of an *index-guided mode*. The optical confinement arises from the difference in the average refractive indices in the waveguide: the line defect acts as the waveguide core, and the photonic crystal lattice with a lower average refractive index acts as cladding.

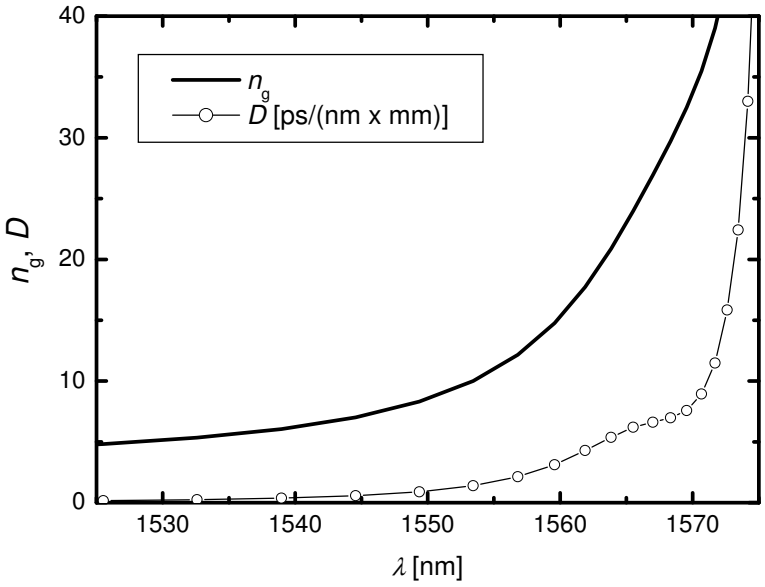

Figure 3.7. Group index n_g and group velocity dispersion parameter D for the fundamental mode in the waveguide of Fig. 3.6 when $a = 408$ nm.

- When approaching the Brillouin zone edge, the slope of the dispersion curve decreases. This part of the mode is confined into the waveguide due to diffraction, and this *bandgap guided mode* has similar properties to the modes in the metallic waveguides. The mode usually has its minimum frequency, the *cut-off* frequency, at the Brillouin zone edge.

Group velocity dispersion

Figure 3.7 shows the group index and the group velocity dispersion parameter [54]

$$D = \frac{\mathrm{d}}{\mathrm{d}\lambda}\left(\frac{1}{v_g}\right) = \frac{1}{c}\frac{\mathrm{d}n_g}{\mathrm{d}\lambda} \tag{3.2}$$

as a function of wavelength, with $a = 408$ nm, which yields a cut-off wavelength 1575 nm. The group index diverges to infinity when approaching cut-off, which suggests that photonic crystal waveguides exhibit zero group velocity at the Brillouin zone edge. However, D simultaneously increases, which is harmful in signal transmission systems: the different frequency components of the modulated light propagate at different velocities, which will deteriorate the signal. To increase the bandwidth of the slow-light regime it is also desirable to extend the propagation constant range of the slow mode. Therefore, a number of approaches have been made to realize slow-light structures with tailored dispersion properties. Some ways to achieve desired dispersion properties are finding the optimal waveguide width [40] or modification of the PhC lattice next to the waveguide defect [38, 39, 55].

4 Experimental methods

This Chapter provides an overview on the manufacturing of the samples and describes the characterization methods and equipment used in the experimental work of this thesis. Waveguide loss measurement using the cutback and Fabry-Pérot (F-P) methods is discussed. Paper I presents a new variant of the F-P characterization method for PhCWs with short length (< 50 μm) inserted between strip waveguides. Finally, this method is applied to W3 waveguides manufactured on the SOI substrate.

4.1 Sample processing

A schematic sample layout is shown in Fig. 4.1. In order to have chips of a reasonable size for optical characterization and easy handling, the photonic crystal waveguides were patterned into 20x20 mm^2 chips with access strip waveguides. An access waveguide had a 90-degree bend to prevent detection of light that was not coupled into the waveguide.

The PhCWs were manufactured on 4-inch SOI wafers produced by Soitec. The buried oxide thickness is 3 μm. A relatively thick buried oxide was used to prevent optical field leakage into the substrate with a high refractive index. A 30 nm thick thermal oxide layer was grown onto the wafers for a hard mask for etching. The device layer thickness after the oxidation was 240 nm.

The SWs, which typically had a width of 5 μm, were patterned using photolithography and reactive ion etching. The oxide mask was etched in a mixture of CF_4 and He. The silicon was subsequently etched in Cl_2+He. After the SW process, the wafer was diced into chips.

A 320 nm thick layer of polymethyl methacrylate (PMMA) was spun onto the SOI chips. The PhCWs and SW tapers were written into the PMMA with a LEO 1560 scanning electron microscope, which had been converted into an EBL system. The writing field was 400x400 μm^2. After lithography and developing the resist in a mixture of de-ionized water and isopropanol, the PhC pattern was transferred first into the SiO_2 mask and subsequently into the silicon layer by similar etching

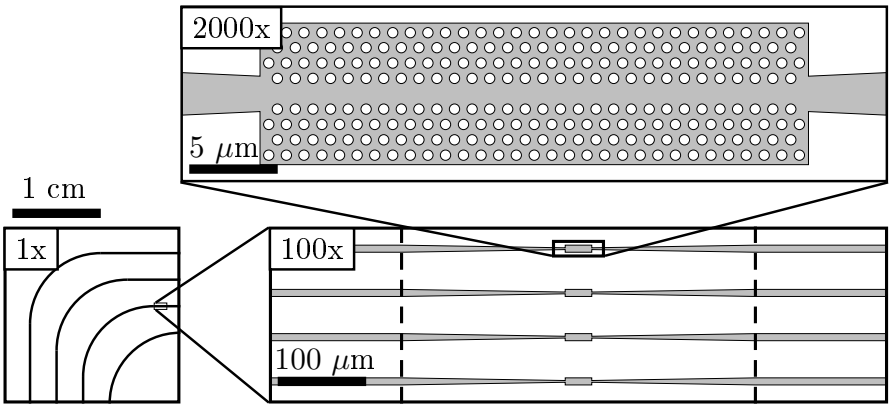

Figure 4.1. Schematic of a typical sample layout. The whole chip with the insertion waveguides is shown in its actual size (1x). The e-beam patterned area with the tapers and the PhCWs is the area between the dashed lines in the 100x magnified image. The PhCW is shown in 2000x magnification.

processes as for the SWs.

Finally, the chip facets with waveguide ends were mechanically polished using diamond lapping films. The smallest grit size used in the lapping was 100 nm.

4.2 Transmission measurements

4.2.1 Measurement setup

For transmission measurements, the device under test was end-coupled with fibers to the source and detector. The fibers were aligned to the sample with manual precision positioners. The devices are polarization sensitive and usually designed for the TE polarization. Therefore, a polarizer and a polarization maintaining (PM) single mode fiber were used in the input. The polarization axes of the PM fiber were aligned prior to the measurement using a polarizer plate. The measured TE/TM mode extinction ratio was more than 20 dB with the optimal alignment. A multimode fiber was used in the output to maximize the collection efficiency and to provide easier alignment than the single-mode fiber.

In most experiments, a tunable laser (Photonetics "Tunics") was used as the light source and an fiber-coupled photodetector (HP 81531A) was used to measure the collected optical power. In a typical spectral measurement, the wavelength is scanned from 1525 to 1625 nm with a wavelength step of 5 pm, which is small enough to resolve the F-P oscillations arising from the reflections at the chip ends.

4.2.2 Loss determination

The output power P is a function of waveguide length L:

$$P(L) = P_{\text{in}} \cdot \eta \cdot \mathrm{e}^{-\alpha L}, \tag{4.1}$$

where η takes into account all the losses in the measurement setup and the waveguide loss coefficient α is in units 1/unit length. A common problem in the waveguide loss measurement is the separation of the waveguide loss from the losses that arise in the measurement setup, particularly in the coupling between the fibers and the chip.

Cutback method

A simple way of canceling out the setup-related losses is the *cutback measurement*, where a set of identical waveguides of different length is measured. In principle, α can be simply obtained from the linear regression of $\ln(P)$ as a function of the waveguide length.

While the cutback measurement is a straightforward method of loss determination, it exhibits some considerable error sources. The method relies on the repeatability of individual transmission measurements, therefore any deviation in the quality of the waveguides or in coupling causes inaccuracy in the loss figure. This problem may be tackled with an extremely long waveguide, which diminishes the effect of the inaccuracies [56]. One may also try to statistically assess the error by using a large number of samples [57]. The reflections at the chip ends cause Fabry-Pérot oscillations into the transmission spectra, which further reduce the repeatability of the transmission measurement. On the other hand, the oscillations make it possible to characterize the waveguide with the *Fabry-Pérot method*.

Fabry-Pérot method

The transmission spectra with the F-P oscillations has a shape [58]

$$T_{\text{FP}} = \frac{t_1^2 t_2^2}{1 + r_1^2 r_2^2 e^{-4\alpha L} + 2 r_1 r_2 e^{-2\alpha L} \cos(4\pi L_{\text{opt}}/\lambda + \phi)}, \tag{4.2}$$

where L and L_{opt} are the physical and the optical lengths of the waveguide, $t_{1,2}$ and $r_{1,2}$ are the transmissitivities and reflectivities at the ends of the waveguide,

respectively, and ϕ is a slowly varying function of λ, which takes into account the phase shifts in the mirrors. T_{FP} oscillates between the values

$$T_{\mathrm{R}} = \frac{t_1^2 t_2^2}{(1 - r_1 r_2 e^{-2\alpha L})^2} \tag{4.3}$$

and

$$T_{\mathrm{A}} = \frac{t_1^2 t_2^2}{(1 + r_1 r_2 e^{-2\alpha L})^2}. \tag{4.4}$$

The waveguide loss can therefore be deduced from the amplitude of the oscillations using the identity

$$r_1 r_2 e^{-2\alpha L} = \frac{\sqrt{T_{\mathrm{R}}/T_{\mathrm{A}}} - 1}{\sqrt{T_{\mathrm{R}}/T_{\mathrm{A}}} + 1}. \tag{4.5}$$

If the reflectivities are known, loss can be calculated directly using Eq. 4.5. It is also possible to use a set waveguides with different length and linear regression of the logarithm of Eq. 4.5. The F-P oscillations also reveal the group index of the mode. It is

$$n_{\mathrm{g}} = L_{\mathrm{opt}}/L = \frac{\lambda_1 \lambda_2}{2L(\lambda_1 - \lambda_2)}, \tag{4.6}$$

where λ_1 and λ_2 are the wavelengths of adjacent oscillation peaks.

4.3 Enhanced Fabry-Pérot method

In the case of PhC waveguides with access strip waveguides, the cutback method is not always practical because deviations in the coupling efficiency and loss in the access waveguides may be larger than the loss over the short PhC waveguide. Parasitic reflections also occur at the various interfaces along the light path, which may further affect the precision of transmission measurements. The problem becomes even more complex in the case of a multimode PhCW, which can transmit the high-order modes that are possibly generated in its input. In this Section, a new type of an F-P method to characterize short PhCWs is presented. In this method, the reflection in the SW-PhCW interface is increased to create a three-cavity system. Using the Fabry-Pérot oscillations of these three cavities, the loss in the PhCW is estimated. The method differs from the conventional Fabry-Pérot method in the sense that no anti-reflection coatings are required on the sample facets. The method is applied to multimode W3 PhCWs fabricated on the SOI substrate.

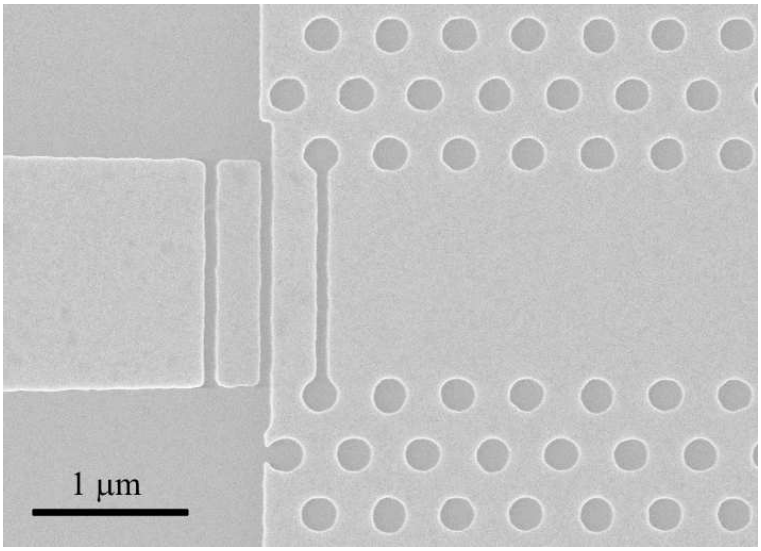

Figure 4.2. Scanning electron micrograph of the interface between the strip waveguide and the W3 waveguide. The Bragg mirror is made of three 90 nm wide grooves with a period of 375 nm.

4.3.1 Sample design and fabrication

The waveguides in this study are of W3 type. The waveguides were patterned onto SOI wafers with top silicon layer thickness 240 nm using the process described earlier in this Chapter. The pitch a of the PhC lattice is 450 nm and the hole diameter is 220 nm.

Figure 4.2 shows a SW-PhCW interface in a processed sample. The three waveguide lengths used were $40a$, $60a$ and $80a$, corresponding to physical lengths 18, 27 and 36μm, respectively. The PhCWs have Bragg mirrors at their both ends. Bragg mirrors are used instead of PhC mirrors to prevent generation of high-order modes in the multimode W3 waveguides. The mirrors were placed at the ends of the PhCW to ensure that all the parasitic reflections at SW-PhCW interface arise in the vicinity of the mirrors. The Bragg mirrors consist of three grooves with a period of 375 nm. The width of the grooves is 90 nm. The FDTD simulations predict Bragg mirror reflectivity of at least 97 % in the wavelength range of the measurement.

4.3.2 Transmission spectrum

The transmission spectrum of a sample with a PhC waveguide length of $40a$ is shown in Figure 4.3. The transmission spectrum shows oscillations with various frequencies. The origin of different oscillations can be easily distinguished from each other because the physical lengths L_{in}, L_{out} and L_{PhC} of the input, output and PhC waveguides were chosen in such a way that $L_{\mathrm{in}} >> L_{\mathrm{out}} >> L_{\mathrm{PhC}}$. The

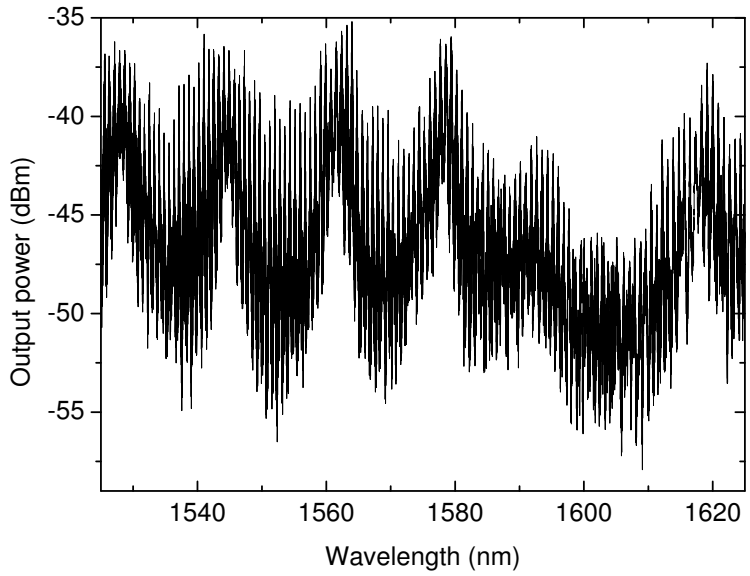

Figure 4.3. The transmission spectrum of a sample with a PhC waveguide with a length of $40a$.

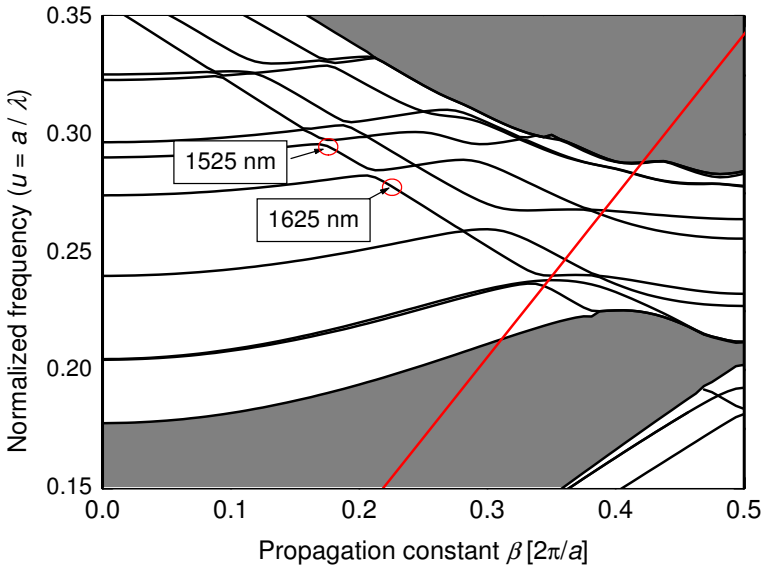

Figure 4.4. 2D PWE simulated dispersion diagram of the waveguide under study. The frequency range of the optical measurement is marked into the fundamental mode.

transmission dip around 1600 nm is seen in the spectra of all three waveguides.

Figure 4.4 shows the dispersion diagram of the TE modes of the waveguides, simulated with the PWE method in 2D using the effective index of 2.84. This effective index corresponds to an SOI structure with a 240 nm thick device silicon layer and 30 nm of mask SiO_2 on top of that, with the wavelength 1.55 μm. The W3 waveguides are multimode at this wavelength. Several *mini-stopbands* [59] are seen at

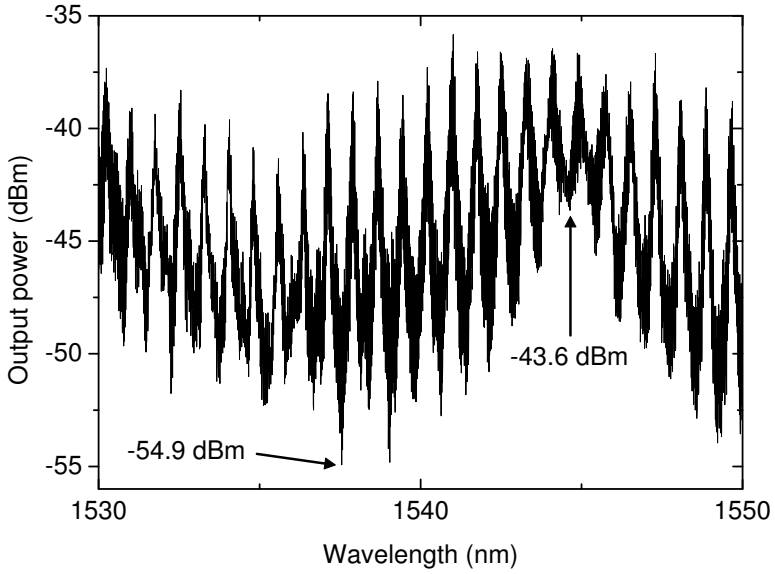

Figure 4.5. Part of the spectrum of Figure 4.3.

the intersections of counter-propagating modes with the same parity. The ends of the wavelength range of the measurement are marked into the dispersion curve of the fundamental mode, which is expected to be best coupled to the input. The dip in the transmission occurs at the frequency of mini-stopband in the fundamental mode, which confirms that the fundamental mode is dominant in transmission. At the wavelength range of the spectrum the mode is index-guided and above the light line.

4.3.3 Fabry-Pérot analysis

The large-period oscillations between 1525 nm and 1590 nm are attributed to the short F-P cavity formed into the PhCW between the Bragg mirrors. The period of these oscillations corresponds to a group index of about 3.8.

The transmission spectrum $P(\lambda)$ has the shape determined by Eq. 4.2 with the exception that it has the short-period oscillations, which arise from the F-P cavity effect in the insertion waveguides. Eq. 4.2 is therefore assumed to be valid when $t_{1,2}$ and $r_{1,2}$ are replaced by the wavelength dependent transmissitivities and reflectivities of the F-P cavities formed into the input and output waveguides, therefore the output power spectrum has a shape

$$P(\lambda) \propto \frac{t_{\mathrm{in}}^2 t_{\mathrm{out}}^2}{1 + A^2 + 2A\cos(4\pi L_{\mathrm{opt}}/\lambda)}, \tag{4.7}$$

where

$$A = r_{\mathrm{in}} r_{\mathrm{out}} e^{-2\alpha L}, \tag{4.8}$$

and $t_{\mathrm{in}}(\lambda)$, $t_{\mathrm{out}}(\lambda)$, $r_{\mathrm{in}}(\lambda)$ and $r_{\mathrm{out}}(\lambda)$ are the transmissitivity and reflectivity spectra of the input and output waveguides, respectively. The transmissitivity and reflectivity of the input waveguide, $t_{\mathrm{in}}(\lambda)$ and $r_{\mathrm{in}}(\lambda)$, respectively, have a period which corresponds to the optical length of the input SW, whereas the periods of $t_{\mathrm{out}}(\lambda)$ and $r_{\mathrm{out}}(\lambda)$ correspond to the optical length of the output SW.

The most interesting points in the $P(\lambda)$ are the points marked with arrows in Fig. 4.5, which is a part of the spectrum of Fig. 4.3. The points are the transmission minima near the resonance and antiresonance of the PhCW. They correspond to simultaneous antiresonance of the cavities formed by the input and output waveguides. At these points the reflectivities r_{in} and r_{out} are at their maximum, yielding the maximal F-P contrast.

The loss in the waveguide can be solved using Eq. 4.5 as in the conventional F-P method, either with a theoretical value for the reflectivity or by measuring cavities of different lengths. The latter method is used here, and it yields an optical loss value of 164 dB/mm. Such high loss is typical for SOI photonic crystal waveguide modes above the light line (see e.g. [52, 53]). For the modes below light line in W1 waveguides fabricated on SOI, the loss is typically two orders of magnitude lower [18, 25].

The advantage of the method presented here is that the parasitic and to some extent non-preventable reflections in the chip ends are utilized in enhancing the F-P effect: the 3 dB loss over the PhCW of length $40a$ resulted in an F-P contrast of 11 dB, compared to 7 dB with the conventional method which involves cancellation of the resonances from the insertion waveguides. Another advantage of the method is that no antireflection coatings are needed at the ends of the chip. No smoothing of the spectra is needed either.

A waveguide of the same type has been studied by Gersen et al. using time-resolved near-field scanning optical microscopy (NSOM) [28]. The NSOM measurements yielded a very similar dispersion diagram to Fig. 4.4 and imaged an extremely slow higher-order mode near the Brillouin zone edge. However, the spectrum in Fig. 4.3 shows that the fundamental mode is the one that has the main contribution on the waveguide transmission when coupled to strip waveguides.

5 2D photonic crystals with ring-shaped holes

Figure 5.1 shows a schematic of a photonic crystal with ring-shaped holes (RPhC). In paper IV, the properties, patterning and applications of such photonic crystals are discussed. In paper III, the ring dimensions of the RPhC are optimized so that W1 waveguides show a wavelength regime with a relatively high and constant group index. Paper V shows a design of an efficient RPhC waveguide coupler into such mode and presents discussion on the coupling. Fabrication and characterization of an SOI based RPhC waveguide (RPhCW) is reported in paper II.

5.1 Properties

5.1.1 Structure

The ring geometry is defined by its inner and outer radii R_{in} and R_{out}. The geometry of the lattice point is defined by two parameters instead of only one, which is the case with circular holes. The air fill factor f_{air} of the RPhC is

$$f_{\text{air}} = \frac{2\pi}{\sqrt{3}a^2}(R_{\text{out}}^2 - R_{\text{in}}^2). \tag{5.1}$$

5.1.2 Bandgap width and center frequency

Figures 5.2 and 5.3 show the 2D PWE simulated bandgap width and center frequency, respectively, as a function of R_{out} for different values of f_{air}. An effective index $n_{\text{eff}} = 2.84$ was used, corresponding to 240 nm of silicon on SiO_2. The bandgap width and center frequency for a conventional PhC with a hole radius R_{out} are plotted as dots into Figs. 5.2 and 5.3 for reference.

At low air-fill factors ($f_{\text{air}} < 30\%$) a larger photonic bandgap can be obtained in a RPhC compared to a conventional PhC with the same f_{air}. Small air-fill factor is

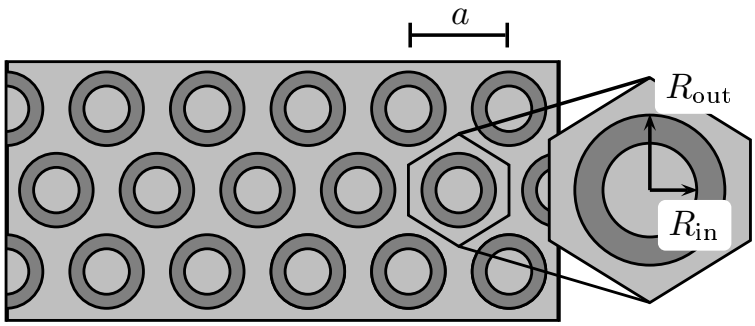

Figure 5.1. Schematic image of an RPhC.

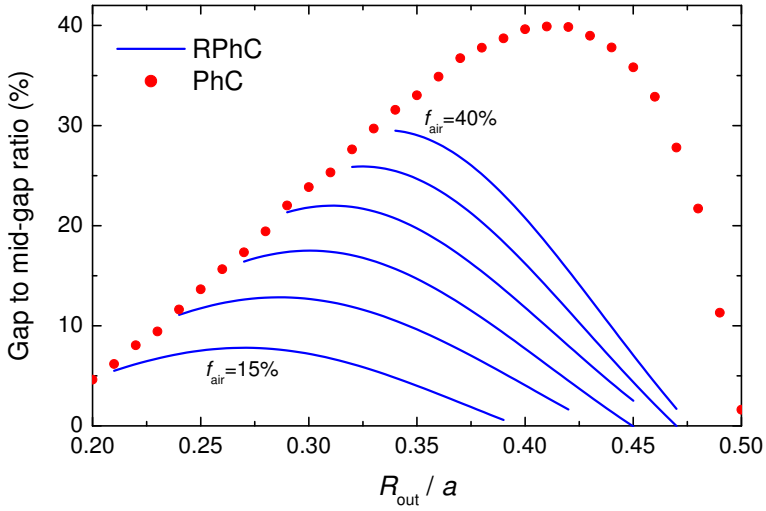

Figure 5.2. Bandgap width of an RPhC as a function of ring outer radius R_{out} at different air fill factors. The scatter plot corresponds to a conventional PhC. The effective index used in the 2D calculation is 2.84.

desired in 2D PhCs, because out-of-plane light scattering decreases with decreasing f_{air} [60]. In Fig. 5.3 it can be seen that the bandgap center frequency is higher for the RPhC than for the conventional PhC with the same f_{air}. The increase of bandgap frequency indicates that a larger part of the mode resides in the air regions.

5.2 Dispersion engineering of waveguides

The reduced group velocity near the Brillouin zone edge enhances light-matter interaction and nonlinearities, which may be utilized in realizing more compact integrated optics devices [25, 28–30, 32]. However, the slow modes usually have a very high group velocity dispersion (GVD). Therefore it is important to realize slow-light structures with tailored dispersion properties. A number of approaches has been

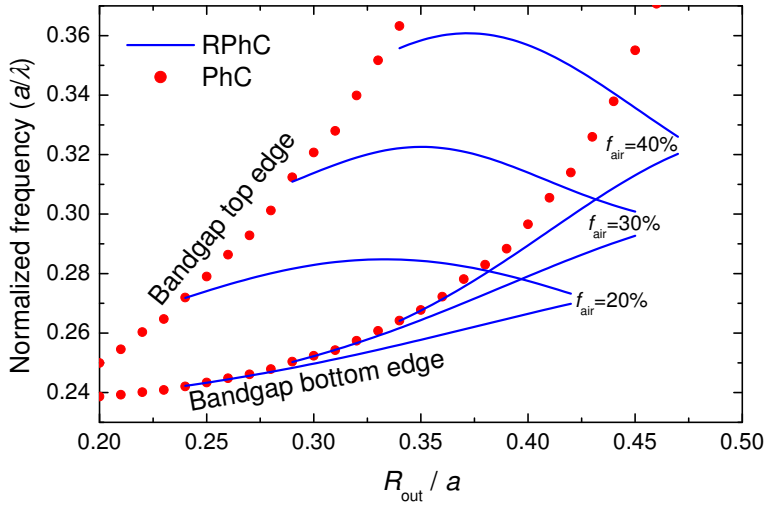

Figure 5.3. Bandgap top and bottom edge frequencies of an RPhC as a function of ring outer radius R_{out} at different air fill factors. The scatter plot corresponds to a conventional PhC. The effective index used in the 2D calculation is 2.84.

used to achieve this, for example using W2 waveguides [40] or modification of the hole radius [38] or period [39] in the first one or two hole row(s) next to the waveguide channel. This Section presents dispersion tailoring of RPhC waveguides using the W1 geometry with no such modifications.

5.2.1 Group velocity

As seen in Fig. 5.3, the bandgap bottom edge frequency of the RPhC increases with increasing R_{out}. Figure 5.4 shows the dispersion diagrams of the bandgap bottom edge and the even W1 waveguide mode in RPhCWs with different values of R_{out}, when $R_{\text{out}} - R_{\text{in}}$ is kept constant at $0.14a$. The effective index used in the 2D calculations is 2.84. Both frequencies increase with increasing R_{out}, but the frequency of the waveguide mode increases at a lesser rate than the bandgap edge frequency. Therefore, with $R_{\text{out}} > 0.37a$, the bandgap bottom edge gets close to the guided mode in the dispersion diagram when $0.35(\frac{2\pi}{a}) < \beta < 0.4(\frac{2\pi}{a})$.

In the vicinity of the bottom band edge, the dispersion curve of the guided mode tends to increase its frequency. Consequently, the dispersion relation of the RPhCW with $R_{\text{out}} = 0.38a$ shows a nearly constant slope between $\beta = 0.35(\frac{2\pi}{a})$ and $\beta = 0.45(\frac{2\pi}{a})$, i.e. the waveguide has a region of a nearly constant group index (Fig. 5.5).

Slow light in the corrugated waveguides is explained as an interaction between the forward and backward propagating modes. The interaction is at its strongest at the edge of the Brillouin zone, where the group velocity vanishes. When moving

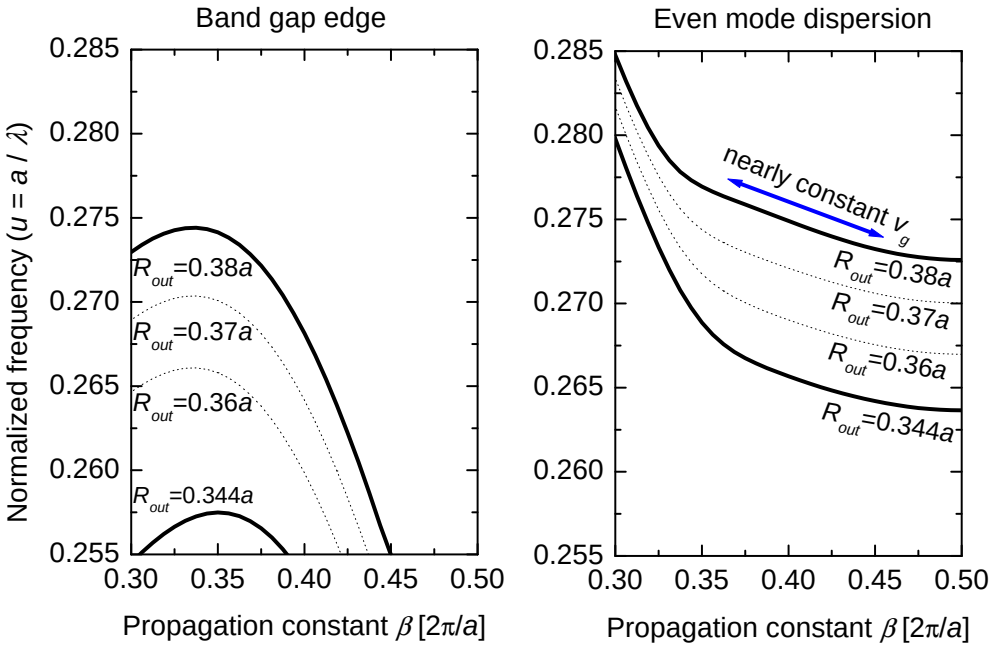

Figure 5.4. Change of bandgap edge and waveguide mode frequencies with the change of ring radius. The width of the ring $R_{\text{out}} - R_{\text{in}}$ is kept constant at $0.14a$. The effective index used in the 2D calculation is 2.84.

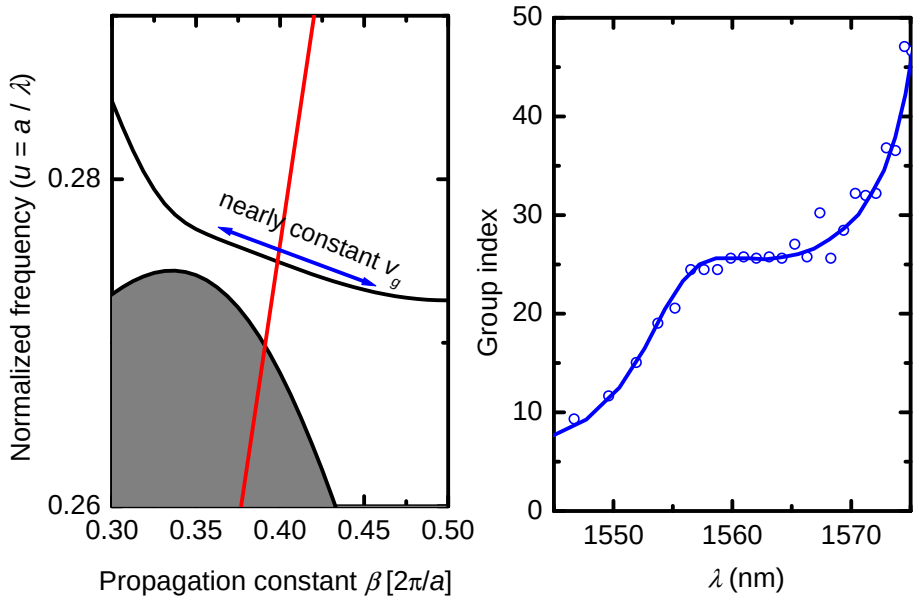

Figure 5.5. Dispersion relation and group index of a W1 RPhCW with a = 430 nm, $R_{\text{out}} = 0.38a$, $R_{\text{in}} = 0.24a$ and $n_{\text{eff}} = 2.84$. The straight line in the dispersion relation graph presents the light line of SiO_2. The scatter plot in the group index graph shows the results of the FDTD simulations.

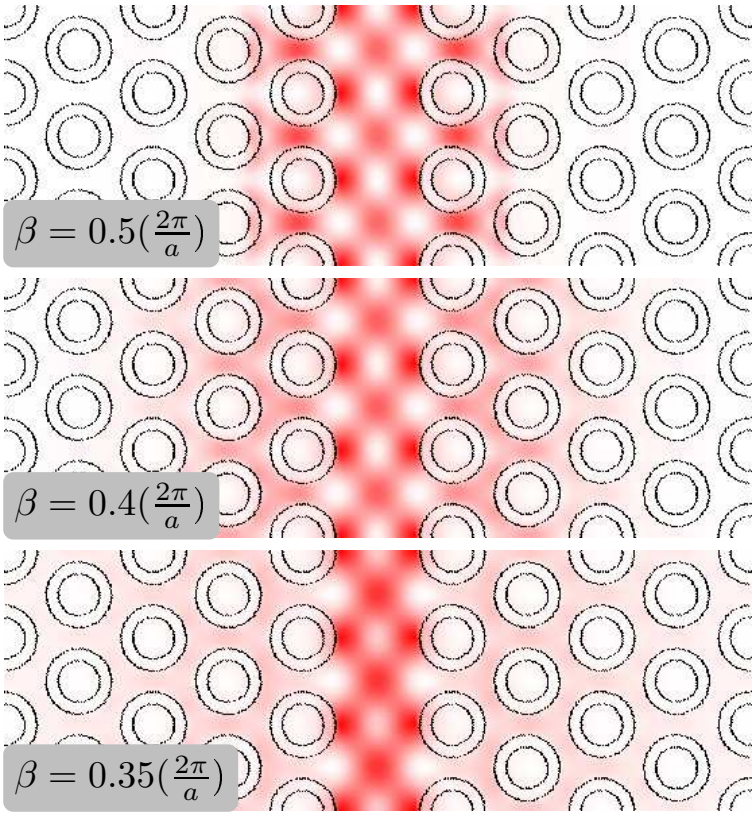

Figure 5.6. Electric field energy densities at three different propagation constants β for the guided mode in Fig. 5.5.

away from the Brillouin zone boundary, the interaction gets weaker due to phase mismatch between the forward and backward propagating modes. However, the mode penetrates deeper into the surrounding RPhC lattice when it is at its closest to the bandgap edge near $\beta = 0.35(\frac{2\pi}{a})$ (see Fig. 5.6). The effect of the periodicity is thus increased, which compensates for the phase mismatch, enabling nearly constant group index over a relatively large wavelength range.

Due to the large mode area, a supercell width of $35a$ was used in the PWE simulations in order to prevent the effect of the periodic boundary conditions. In order to verify the results, the group index was also deduced from the Fabry-Pérot oscillations in the FDTD simulated transmission spectrum. Figure 5.5 shows the dispersion relation and the group index of a W1 RPhCW with R_{out}=0.38a and R_{in}=0.24a. The group index has a quasi constant value of 25 over a wavelength range of 8 nm.

To extend the part of the slow mode that is below the light line, a waveguide with a decreased frequency was designed. The decrease in frequency was realized by increasing the effective index of the silicon slab, i.e., by increasing the silicon layer thickness h. With n_{eff}=3.18, corresponding to h = 400 nm, the slow light region is almost entirely below the light line. Figure 5.7 shows the band diagram and

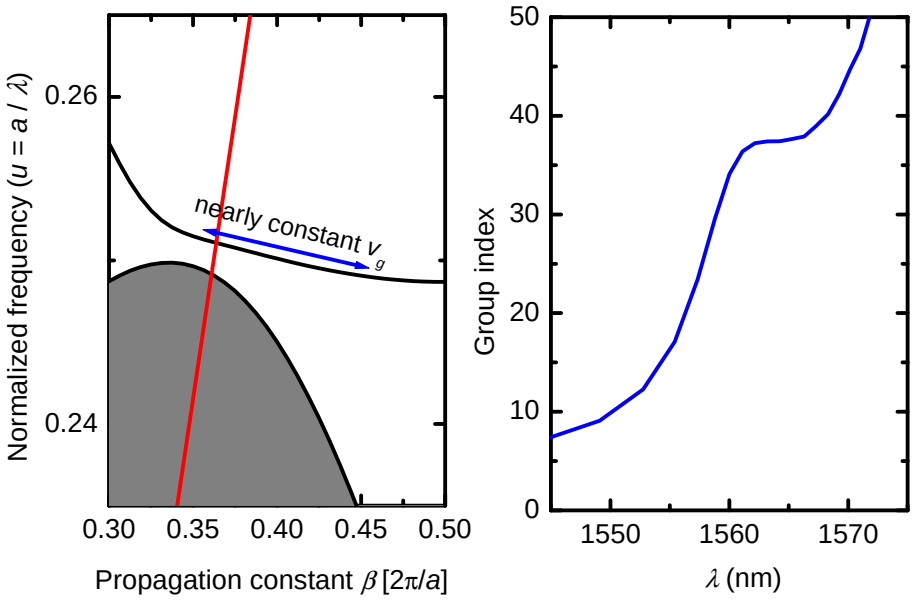

Figure 5.7. Dispersion relation and group index of a W1 RPhCW with a = 392 nm, $R_{\text{out}} = 0.385a$, $R_{\text{in}} = 0.235a$ and $n_{\text{eff}} = 3.18$ (corresponding to a 400 nm thick silicon layer on silica). The straight line presents the light line of SiO_2.

group index of a RPhCW with $R_{\text{out}} = 0.385a$, R_{in}=$0.235a$ and n_{eff}=3.18. Both the bandgap and the mode frequency have dropped compared to Fig. 5.5. The group index is 37 ± 3 over a wavelength range of 8 nm.

5.2.2 Dispersion

As can be seen from the definition of the group velocity dispersion parameter D (Eq. 3.2), nearly constant group index regions exhibit small dispersion. Figure 5.8 shows the GVD calculated from the group index for the RPhCW's in Figs. 5.5 and 5.7. Group velocity dispersion minima can be seen in the nearly constant group index region with $D < 1$ ps/(mm $\cdot$ nm) over 8 nm for the RPhCW of Fig. 5.5 and $D < 1$ ps/(mm $\cdot$ nm) over 3 nm for the RPhCW of Fig. 5.7. In a conventional PhCW, D increases monotonically when coming closer to cut-off wavelength.

The RPhCW with $R_{\text{out}} = 0.344a$, $R_{\text{in}} = 0.203a$ and n_{eff}=2.84, studied in Paper II, shows a dispersion flattened slow-light regime where the GVD parameter is nearly constant at about 4.2 ps/(nm $\cdot$ mm) and n_{g} increases from 20 to 30 over the wavelength range of 5 nm. The dispersion flattened mode exhibits vanishing third order dispersion, which may be important in order to avoid pulse distortion in data processing applications [61].

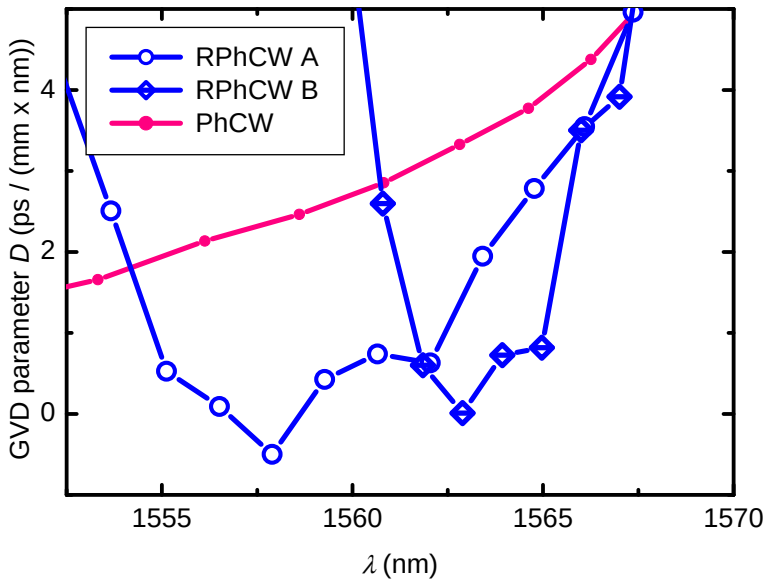

Figure 5.8. Group velocity dispersion calculated from the group index spectra of three waveguides. RPhCW A: $R_{\text{out}} = 0.38a$, $R_{\text{in}} = 0.24a$, $a =$ 430 nm and n_{eff}=2.84, RPhCW B: $R_{\text{out}} = 0.385a$, $R_{\text{in}} = 0.235a$, $a = 392$ nm and n_{eff}=3.18. The curve with closed dots corresponds to a conventional PhCW with $R = 0.278a$, $a = 400$ nm and n_{eff}=2.84. Lattice constants are chosen so that the cut-off wavelength is 1575 nm for all three waveguides.

5.2.3 3D simulation

Fig. 5.9 shows the 3D PWE simulated band diagram and group index corresponding to the 2D simulated graphs of Fig. 5.7. The silicon slab thickness h used in the calculations is $1.02a$ and the lattice constant used to determine the wavelengths is $a = 400$ nm. The dispersion curve has a very similar shape to the 2D simulated curve. However, the quasi constant group index is about 55 and its wavelength range is 5 nanometers. The group index values calculated with 3D simulations are thus higher than those calculated in 2D. The difference arises from the high waveguide dispersion of the SOI substrate. The effective index is defined for a definite frequency. At lower frequencies, the value for n_{eff} is higher than the actual effective index, therefore the mode is at lower frequency than the real 3D mode, and vice versa, the high-frequency modes are higher in the calculations made with the effective index approximation. Therefore, the slope of $\omega(\mathbf{k})$ in the real 3D case decreases, i.e. n_{g} is slightly higher than the 2D simulations suggest. Otherwise the differences between the 2D and 3D simulated dispersion relations are small. The effective index approximation thus gives a good picture on the dispersion relation of the real 3D device on SOI, as long as the waveguide dispersion of the slab is taken into account.

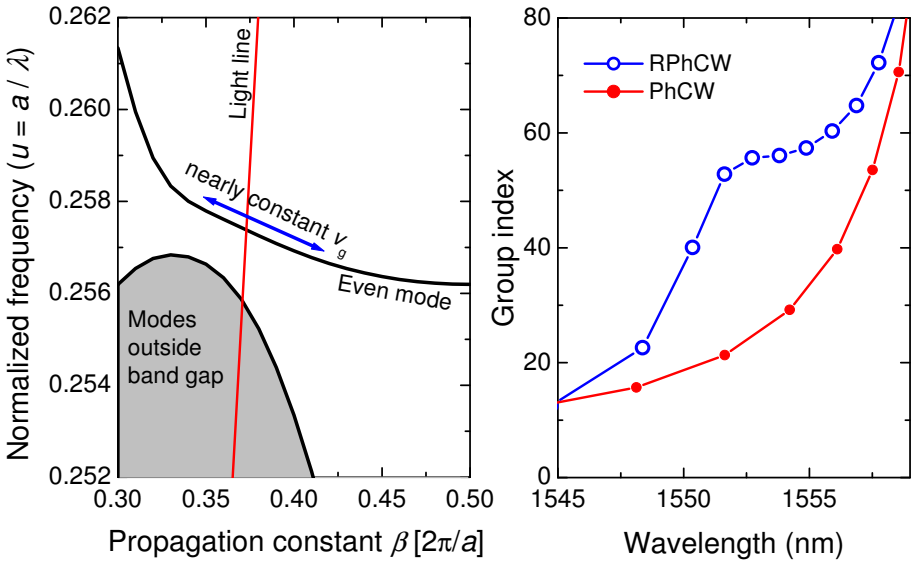

Figure 5.9. 3D simulated dispersion relation and group index in a W1 RPhCW with $a = 400$ nm, $R_{\text{out}} = 0.385a$ and $R_{\text{in}} = 0.235a$. Group index in a W1 PhCW with $a = 375$ nm and $R = 0.305a$ is plotted for reference. For both waveguides, $f_{\text{air}} \approx 34\%$, $n_{\text{Si}} = 3.45$ and the slab thickness $h = 1.02a$.

5.3 Coupling into the slow mode

Efficient coupling between waveguides with different group velocities is not trivial [34, 42, 43, 62]. Transmission from strip waveguides (SWs) to slow modes in PhCWs has been improved by optimizing the termination of the PhCW [62], tapering the PhCW [43] and by using high group velocity PhCWs at both ends of the slow light PhCW [41, 42, 63]. These studies demonstrate highly efficient couplers where light is slowed down inside the PhCW in an extremely small length compared to what is required for adiabatic mode conversion. The efficient coupling was explained by F-P resonances in [63]. In [41] it was shown that a transient zone with a length of a few lattice periods appears at the interface between PhCW sections of different group velocities. In this region, light is smoothly slowed down as it penetrates the slow-light waveguide. Using the RPhCW, such a coupler can be conveniently combined with a dispersion tailored slow-light waveguide.

5.3.1 Coupler design

Figure 5.10 shows the dispersion relation of the dispersion tailored slow mode of Fig. 5.7 as a thick line and dispersion relations of RPhCWs with slightly different values of R_{out} as thin lines. The ring width is kept constant at $R_{\text{out}} - R_{\text{in}} = 0.15a$. The frequency range corresponding to the nearly constant v_{g} is highlighted

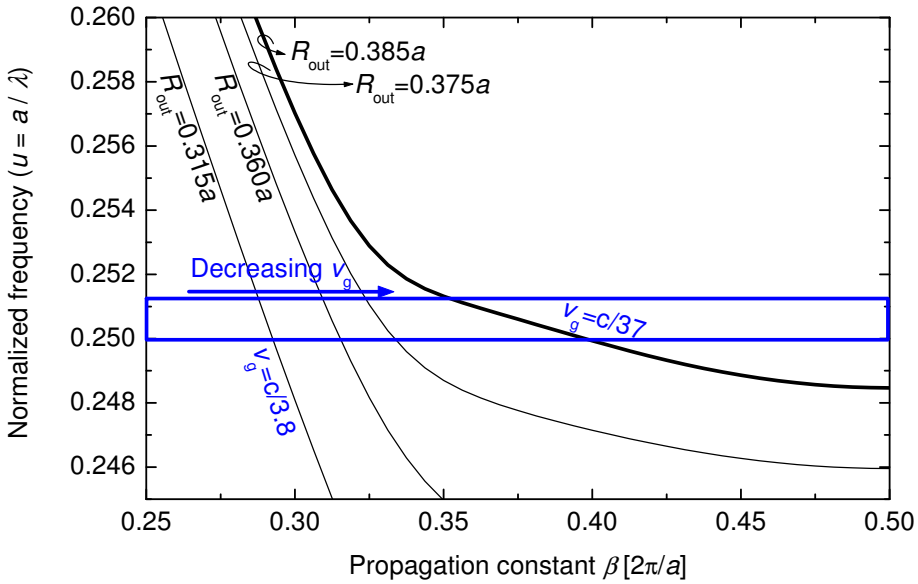

Figure 5.10. Dispersion relation of the even mode in RPhCWs with n_{eff}=3.18, $R_{\text{out}} - R_{\text{in}} = 0.15a$ and with different outer ring radius R_{out}. In the normalized frequency range within the frame, the average group velocity decreases from $v_{\text{g}} = c/3.8$ when $R_{\text{out}} = 0.315a$ to $v_{\text{g}} = c/37$ when $R_{\text{out}} = 0.385a$.

in Fig. 5.10.

For all waveguides in Fig. 5.10, the even mode is in the index-guided regime with $v_{\text{g}} \approx c/3.8$ when $\beta < 0.32(\frac{2\pi}{a})$. When approaching the Brillouin zone edge at $\beta = 0.5(\frac{2\pi}{a})$, the mode becomes bandgap guided: v_{g} decreases and eventually vanishes when $\beta = 0.5(\frac{2\pi}{a})$. If R_{out} is decreased, the air-fill factor of the RPhCW decreases, therefore the dispersion curve of the guided mode is shifted to smaller frequencies. Consequently, the average group velocity within the frequency range of interest can be changed from $v_{\text{g}} = c/3.8$ with $R_{\text{out}} = 0.315a$ to $v_{\text{g}} = c/37$ with $R_{\text{out}} = 0.385a$.

Figure 5.11 shows the coupler design. The slow-light waveguide is sandwiched between two couplers, which are RPhCWs with $R_{\text{out}} < 0.36a$ and are coupled with strip waveguides. The transmission T of the device is simulated using FDTD simulations using a device and source-detector configuration sketched into Fig. 5.11. As the first step in the coupler design, transmission from SWs to the couplers is optimized. The SW width and termination point of the RPhCW (denoted as parameters w and d in the inset in Fig. 5.11) are important in the SW-PhCW coupling and they are optimized first. Optimal coupling is obtained with parameters $w = 1.6a$ and $d = 0.625a$.

In Figure 5.12, group velocity at $u = 0.250$ is plotted as a function of R_{out}, together with the transmission through a $10a$ long RPhCW sandwiched between two SWs. For the RPhCW with $R_{\text{out}} = 0.385a$, transmission is only 52% at $u = 0.250$. T

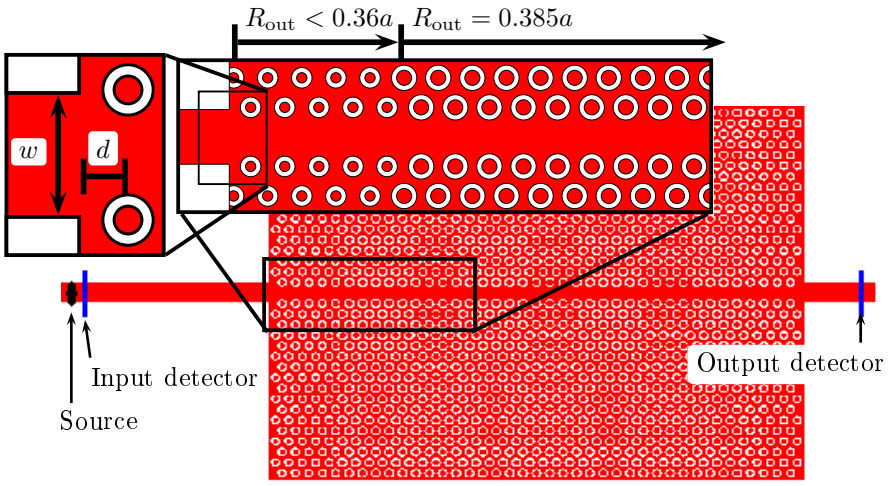

Figure 5.11. Schematic image of the coupler design. A slow-light RPhCW is coupled to SWs through RPhCWs with smaller R_{out}, i.e. with higher v_g. The insets show the beginning of the RPhCW. The source and detector configuration used in the FDTD simulations is also shown in the schematic.

increases with increasing group velocity, being more than 98% when $R_{out} \leq 0.315a$ and $v_g > c/4$. Therefore, $R_{out} = 0.315a$ is chosen for the coupler.

With $n_g < 40$ in the RPhCW, efficient coupling is expected with an abrupt transition between the RPhCW sections [41]. A simple coupler with an abrupt change of R_{out} is therefore chosen. In the initial structure, coupler length of $5a$ is used. The effect of the length of the couplers will be discussed later in this thesis.

Figure 5.13 shows the magnetic field in the input end of the waveguide when it is excited with a continuous wave with a normalized frequency $u = 0.2506$. The conversion from the coupler mode into the wider slow mode takes place within a few lattice periods of the coupler-RPhCW interface, which confirms the existence of a transient zone at the interface. The magnetic field in the slow-light RPhCW is enhanced fy a factor of 3.5 compared to the strip waveguide, i.e. the slow-light device provides a 12.25x increase in intensity. In the next part, the spectral properties of the coupler will be studied.

5.3.2 Transmission properties

Figure 5.14 shows the transmission spectra of a $50a$ long slow-light RPhCW with and without couplers (T_{opt} and T_{ref}, respectively). Transmission through the RPhCW with $R_{out} = 0.315a$ sandwiched between SWs (T_{cpl}) is also plotted in Fig. 5.14 in order to show the transmission between the SWs and the couplers. The PWE calculated group index $n_g = c/v_g$ in the RPhCW with $R_{out} = 0.385a$ from Fig. 5.7

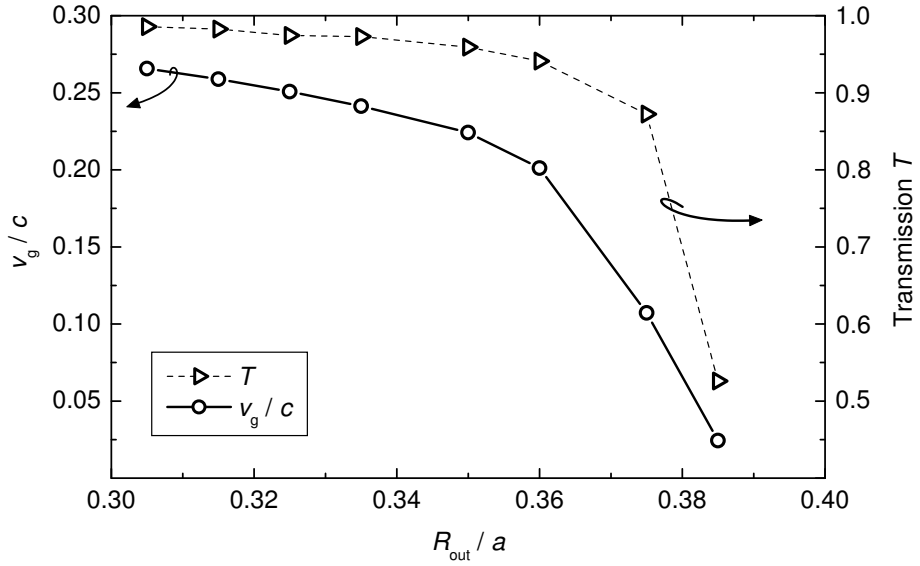

Figure 5.12. Group velocity in the RPhCW (solid line) and the transmission of a $10a$ long RPhCW sandwiched between two strip waveguides (dashed line) as a function of R_{out} at the normalized frequency $u = 0.250$.

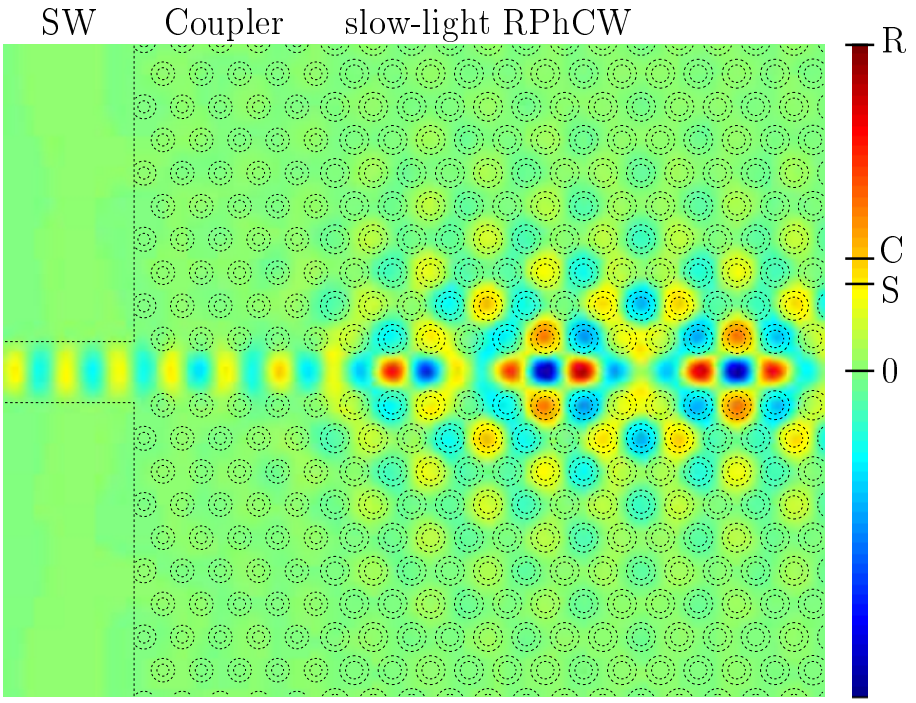

Figure 5.13. The H_y field in the input coupler with a continuous wave source operating at frequency $u = 0.2506$. The zero point and maxima of H_y in the SW (S), coupler (C) and RPhCW (R) are marked onto the colorbar.

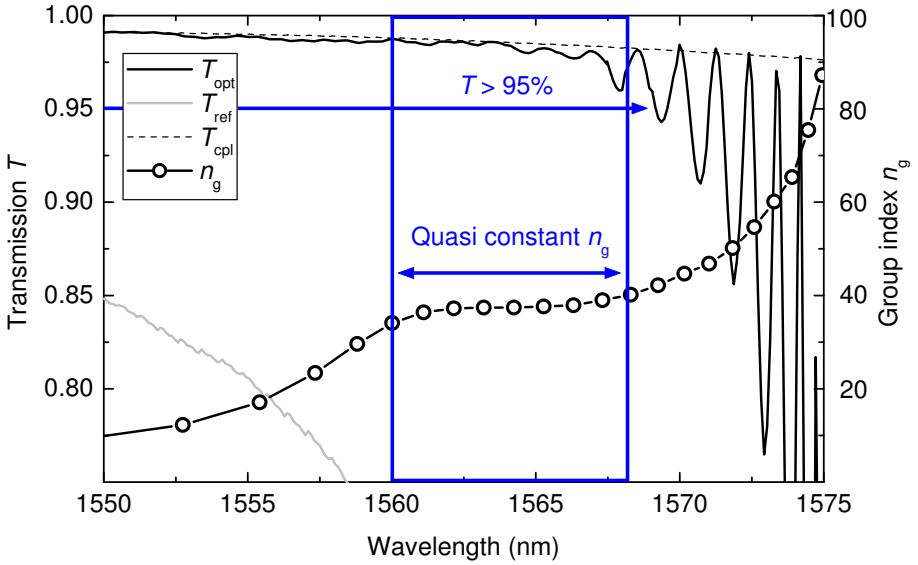

Figure 5.14. FDTD simulated transmission spectra through a $50a$ long RPhC waveguide with $R_{out} = 0.385a$ and $a = 392$ nm, with and without couplers at both ends (T_{opt} and T_{ref}, respectively). T_{cpl} is the transmission spectrum of a $10a$ long RPhCW with $R_{out} = 0.315a$ (i.e., a waveguide similar to the couplers) sandwiched between SWs. Group index $n_g = c/v_g$ is deduced from the PWE simulations of Fig. 5.7.

is plotted in the same graph. All the curves are plotted as a function of wavelength λ with a lattice constant $a = 392$ nm, which yields a cut-off wavelength of 1575 nm.

T_{opt} is higher than 95% over the wavelength range of nearly constant v_g between 1560 nm and 1568 nm. Up to the wavelength 1567 nm, T_{opt} is very close to T_{cpl}. Only small oscillations are seen in the spectrum, with their period varying as a function of the group index of the RPhCW. These oscillations are F-P resonances due to reflections between the two coupler-RPhCW interfaces. These small F-P oscillations are a sensitive indicator of mode conversion efficiency and reflections in the coupler and therefore constitute an efficient way of studying the various coupling mechanisms in such structures.

5.3.3 Mode conversion

PhCW modes within the photonic bandgap are necessarily lossless in 2D simulations, as out-of-plane losses do not exist and in-plane losses are prohibited by the PhC. Therefore, non-ideal transmission in our simulation is induced by in-plane scattering and/or by parasitic back reflection at each waveguide interface.

The transmission of a lossless F-P cavity is equal to unity at resonance [58]. T_{opt}

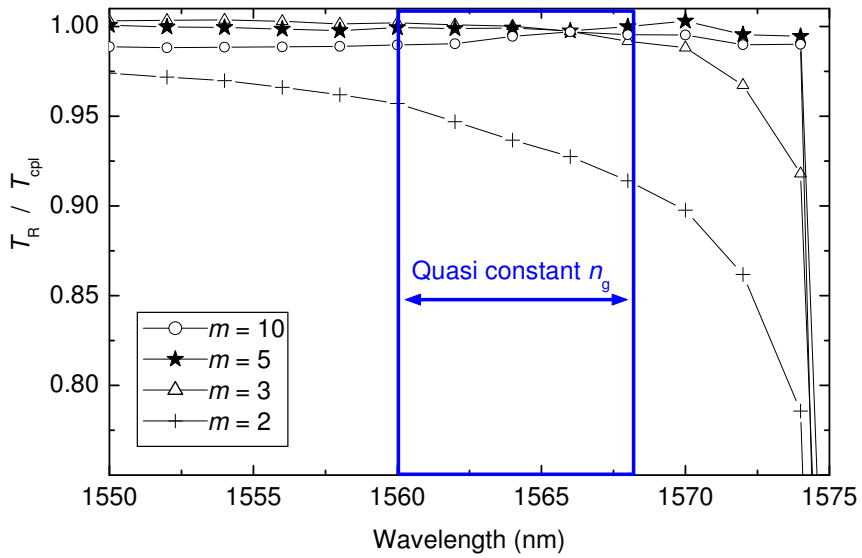

Figure 5.15. A measure for mode conversion efficiency, $T_{\mathrm{R}}/T_{\mathrm{cpl}}$, with different coupler lengths. T_{R} is the linear interpolation between the points corresponding to F-P resonances in the transmission spectra with a coupler with a length of m lattice periods, and T_{cpl} is the transmission spectra of the coupler sandwiched between strip waveguides.

should therefore be equal to T_{cpl} at each resonance, provided that the coupler converts the slow mode properly into the coupler mode; this is the case in the transmission spectrum shown in Fig. 5.14 for wavelengths up to 1572 nm. For resonances at longer wavelengths, $T_{\mathrm{opt}} < T_{\mathrm{cpl}}$, suggesting that mode conversion is not perfect.

To get more insight on the mode conversion along the coupler, the FDTD simulation of T_{opt} is repeated with different coupler lengths m, where m is the coupler length in lattice periods. The results are shown in Figure 5.15 where $T_{\mathrm{R}}/T_{\mathrm{cpl}}$ is plotted for different coupler lengths m; the T_{R} spectra is obtained with the linear interpolation between the points corresponding to F-P resonances in T_{opt}. Perfect mode conversion should yield $T_{\mathrm{R}}/T_{\mathrm{cpl}} = 1$.

The coupler with a length of just $2a$ is enough to improve transmission compared to the waveguide with no couplers (compare to T_{ref} in Fig. 5.14). A coupler with $m = 3$ provides nearly perfect coupling in the quasi constant group index range. With $m = 5$, transmission is enhanced between $\lambda = 1566$ nm and $\lambda = 1574$ nm. Further increase in the coupler length maintains the excellent transmission, which shows that efficient coupling occurs when the evanescent modes excited at the two coupler interfaces do not overlap and interfere destructively [41]. The weak transmission variations that are observed for longer couplers correspond to F-P oscillations in the coupler [63]. The major difference to the coupler reported [63] is that the F-P oscillations are not the main contributor to the coupling in this case. For a coupler

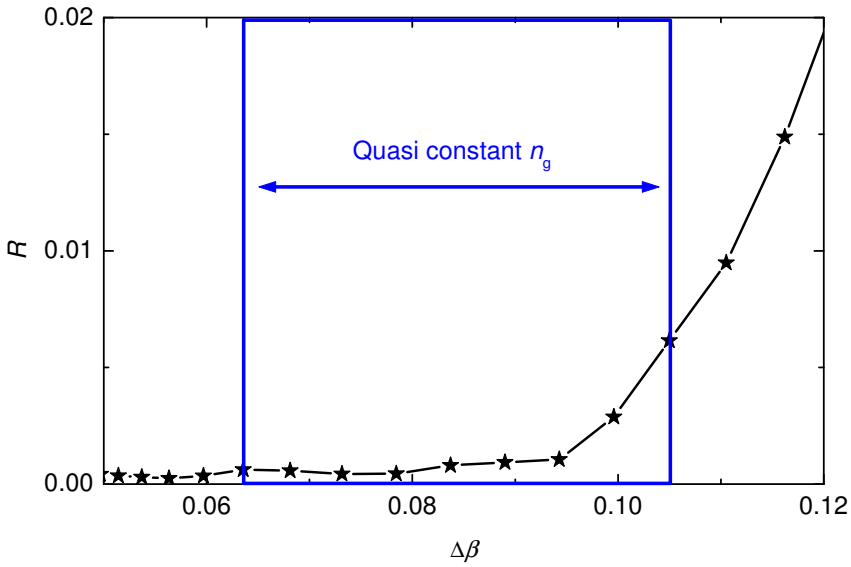

Figure 5.16. Parasitic back-reflectance R as a function of propagation constant mismatch $\Delta\beta$ with a $5a$ long coupler. The wavelength range of the figure is from about 1555 nm to about 1570 nm, the quasi constant n_g region is drawn between 1560 nm and 1568 nm and the scatter symbols have an interval of 1 nm.

length of $5a$, the mode conversion losses are lower than 0.3% in the wavelength range of quasi constant n_g. T_R drops near cut-off for all coupler lengths, indicating that a more complicated coupler might be needed for higher n_g [41, 43].

5.3.4 Back-reflectance

The signature of the back reflections are the F-P oscillations in the transmission spectrum, which can be seen in T_{opt}. In this case, the RPhCW can be regarded as a symmetric, lossless F-P cavity, therefore Eq. 4.5 gets a form

$$R = \frac{\sqrt{T_R/T_A} - 1}{\sqrt{T_R/T_A} + 1}, \tag{5.2}$$

where R is the intensity reflectance at the ends of the cavity.

The amplitude of the F-P oscillations in Fig. 5.14 increases at higher wavelengths already within the nearly constant n_g regime. The oscillation amplitude is indeed a function of the propagation constant mismatch between the slow mode and the coupler mode, $\Delta\beta$. Figure 5.16 shows the back-reflectance as a function of $\Delta\beta$. In the wavelength range with constant n_g, R is lower than 0.6%. Although the back-

reflectance is very low, phase match at the interface between the coupler and the slow-light waveguide was found crucial.

5.4 Applications

The waveguides having a several nm bandwidth with low or constant GVD and with efficient coupling to photonic integrated circuits are particularly attractive in telecommunications and signal processing applications. Such devices are a step toward hybrid photonic circuits, where slow-light waveguides are parts of a photonic chip that may elsewhere be based on strip waveguides. The RPhC exhibits properties that are favorable in other applications as well. In an earlier study it was shown that the RPhC allows some freedom of engineering polarization independent bandgaps [64]. This might enable PhC devices with reduced polarization dependence.

In the next part it will be shown that the RPhC waveguide can be designed to be sensitive to small refractive index variations in the air holes. In that example, the effect is utilized to enhance the sensitivity of an earlier proposed biosensor, which is based on the sensitivity of the cut-off frequency of the PhCW mode on the ambient refractive index [65]. Such effect can be utilized in many other applications by infiltrating the holes with functional materials, e.g. with liquid crystals to make a switch, or with magnetic polymers to realize a polarization converter.

5.4.1 Biosensing

A comparison will be made between cut-off frequencies of an RPhCW and a PhCW, both fabricated into the SOI substrate with $f_{\mathrm{air}} \approx 34\%$ and $\lambda_{\mathrm{co}} \approx 1570$ nm. Consider that the volume above the waveguide and inside the holes is filled with a gas or a liquid with refractive index n_{a}. Figure 5.17 shows the 3D PWE simulated cut-off wavelength λ_{co} in two waveguides as a function of n_{a}. The change in λ_{co} as a function of n_{a} is nearly linear between $n_{\mathrm{a}} = 1.00$ and $n_{\mathrm{a}} = 1.10$. The sensitivity, defined here as the relative cut-off shift $\Delta\lambda_{\mathrm{co}}/\lambda_{co}$ in % induced by an ambient refractive index change $\Delta n_a = 0.01$, is 0.073% for the RPhCW and 0.042% for the PhCW. Thus, the RPhCW is nearly twice as sensitive as the conventional PhCW with the same f_{air}.

Figure 5.18 shows the sensitivity of an RPhCW as a function of R_{out} for different air-fill factors. The sensitivity of a conventional PhCW as a function of the hole radius is plotted in comparison. The 2D PWE simulations were carried out with an effective index $n_{\mathrm{eff}} = 3.18$.

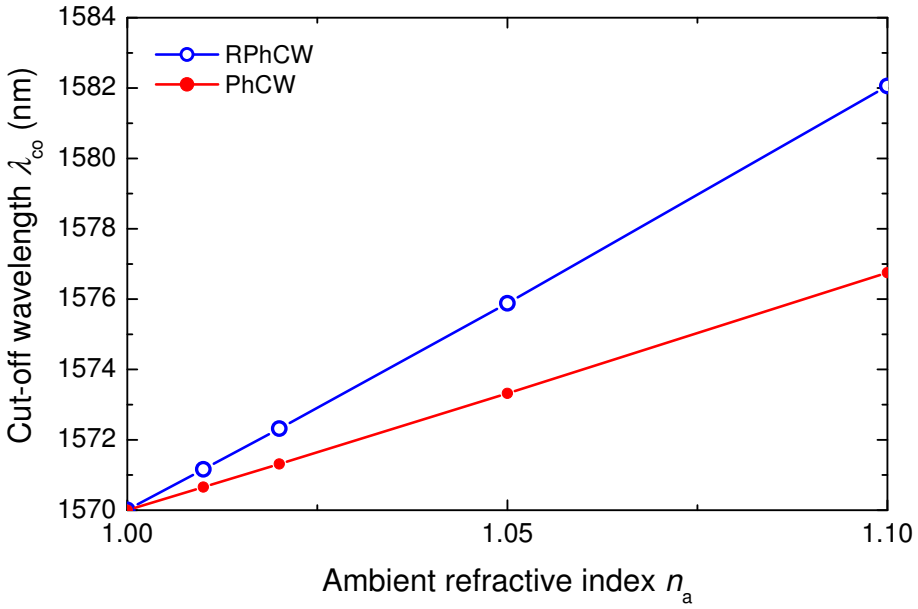

Figure 5.17. Calculated cut-off wavelength as a function of the ambient refractive index n_a for a W1 PhCW and a W1 RPhCW etched in SOI. For the RPhCW: $a = 405$ nm, $R_{out} = 0.385a$ and $R_{in} = 0.235a$. For the PhCW: $a = 380$ nm and $R = 0.305a$. For both waveguides $f_{air} \approx 34\%$ and $h = a$.

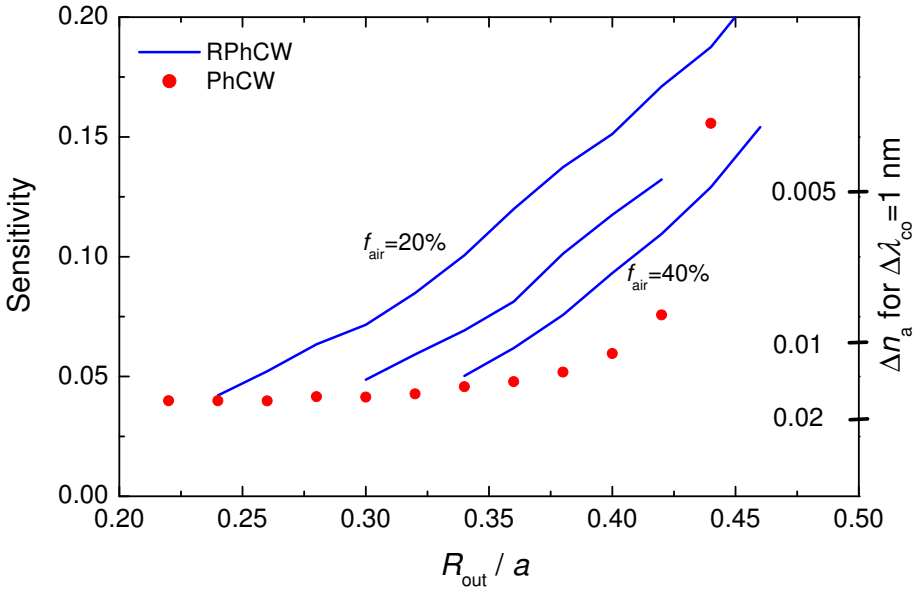

Figure 5.18. Calculated sensitivity in RPhCWs with $f_{air} = 20\%$, 30% and 40%. The dots correspond to a conventional PhCW with hole radius R_{out}. The sensitivity is defined as the relative cut-off shift $\Delta\lambda_{co}/\lambda_{co}$ in % induced by an ambient refractive index change Δn_a equal to 0.01. The ticks on the y axis on the right show Δn_a that induces $\Delta\lambda_{co} = 1$ nm when $\lambda_{co} = 1570$ nm. The 2D PWE simulations were carried out with an effective index $n_{eff} = 3.18$.

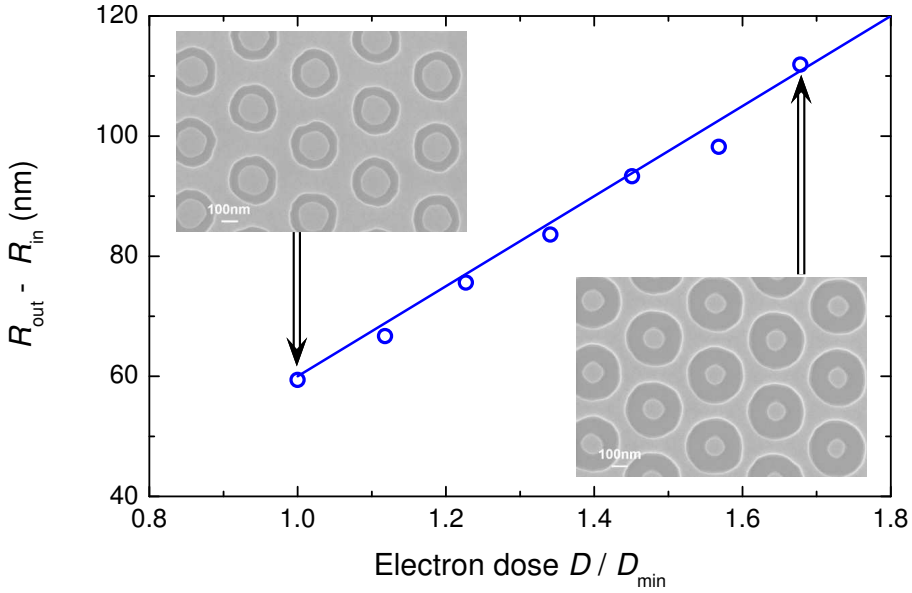

Figure 5.19. Ring width $R_{\text{out}} - R_{\text{in}}$ as a function of the electron dose.

The sensitivity of the conventional PhCW is nearly constant for a hole radius smaller than $0.4a$. For a hole radius larger than $0.4a$, the sensitivity eventually increases. However, PhCs with such large circular holes are difficult to manufacture due to the very thin walls between neighboring holes. In the case of RPhCWs, sensitivity increases with decreasing f_{air} and with increasing R_{out}. In other words the rings should be as narrow as possible for optimal sensitivity. The example of Fig. 5.17 has a ring width $R_{\text{out}} - R_{\text{in}}$ of 60 nm. Such narrow rings can be patterned into the SOI structure with electron beam lithography and reactive ion etching, as will be demonstrated next.

5.5 Experimental

5.5.1 Patterning of ring-shaped holes

Lattices of ring-shaped holes were patterned into an SOI wafer with a process described in Chapter 4. The rings are written as circular lines with the radius $(R_{\text{out}} + R_{\text{in}})/2$. The final R_{out} and R_{in} are determined by the width of the line, which depends on the beam current and the scanning speed of the beam (Fig. 5.19). This method intrinsically minimizes the time of the electron beam lithography. Writing of a field of ring holes takes up to four times less time than writing of a field of circular holes with the same air-fill factor.

An RPhCW with length $L = 40a$ was manufactured using this process. Figure 5.20 shows scanning electron micrograph of the end of a fabricated RPhCW. Silicon is

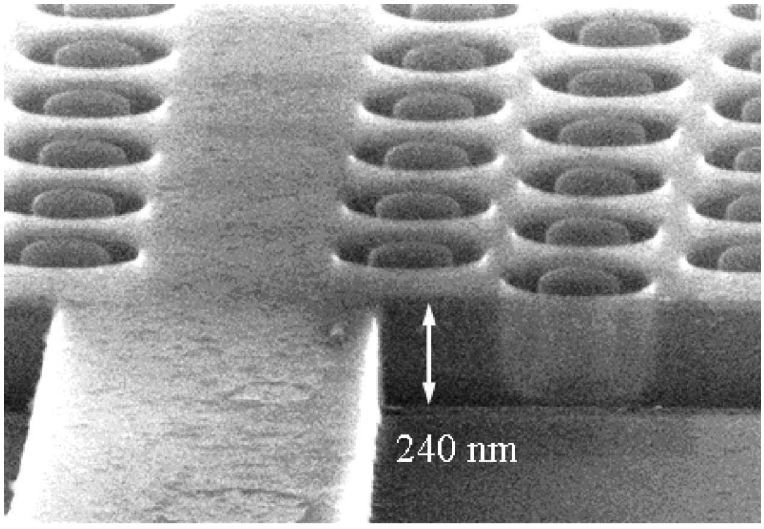

Figure 5.20. Scanning electron micrograph of an RPhCW.

slightly transparent to the electron beam, therefore it is possible to see through the end of the RPhC and notice that the etch profile is nearly perfectly vertical. The lattice parameter of the RPhC is 475 nm and the ring width $R_{\text{out}} - R_{\text{in}}$ is about 65 nm.

5.5.2 Waveguide transmission

The transmission spectrum of the waveguide, recorded with a 5 nm averaging window, is shown on Fig. 5.21. The purpose of the averaging is the removal of the high-frequency oscillations coming from the access strip waveguides. The decrease in transmission observed at around 1570 nm is attributed to the increase of the overall loss in the waveguide as group velocity of the even TE-like mode decreases [66]. Transmission increases again for wavelength above 1630 nm probably due to transmission of TM-polarized light. The F-P oscillations visible in the smoothed spectrum are attributed to the RPhCW. The group index in the RPhCW can be deduced from the F-P oscillation periods using Eq. 4.6.

The measured group index dependence on wavelength is consistent with the PWE simulation (Fig. 5.22). A maximal group index value of 22 is measured. For larger group index, the optical length of the RPhCW is of the same order as the length of the access waveguides, therefore F-P oscillations from the RPhCW are difficult to distinguish from parasitic oscillations.

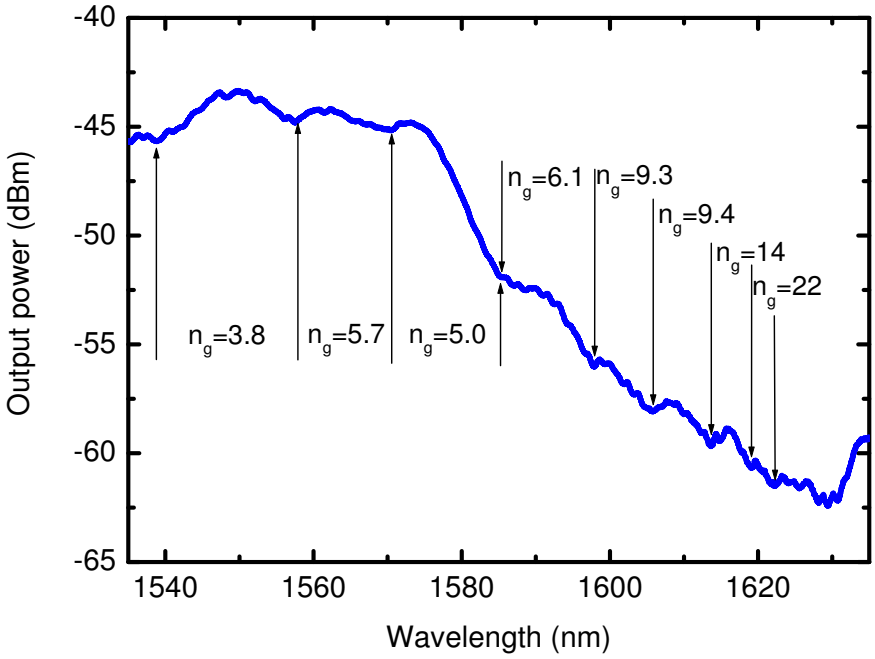

Figure 5.21. Measured transmission spectrum of a $40a$ long RPhCW. Group index values calculated from the Fabry-Pérot oscillation period are indicated.

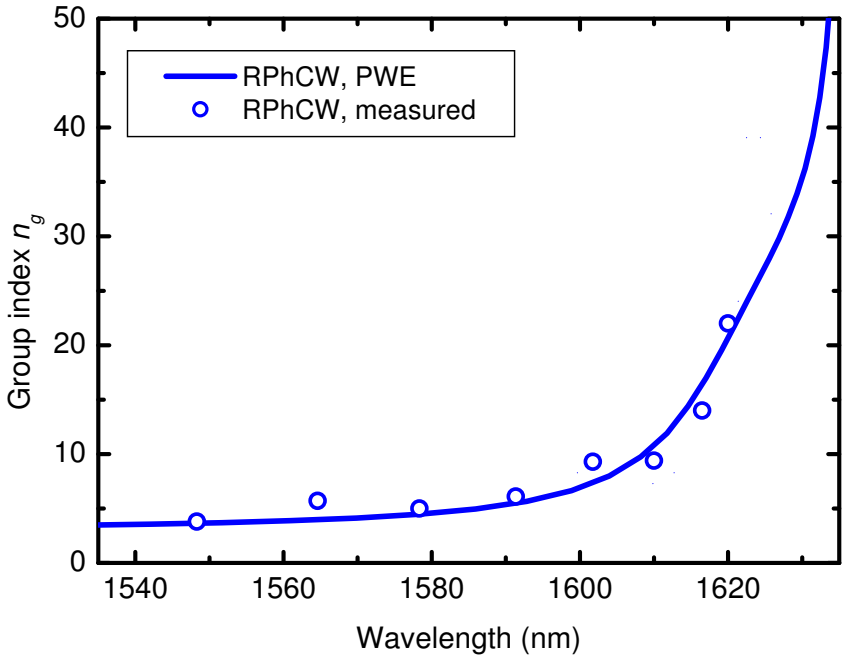

Figure 5.22. Comparison between the measured and simulated group index as a function of wavelength. The wavelength scale of the simulation has been tuned by less than 2% for the best match to the measurement.

6 Summary and outlook

The aim of this study was to design and characterize photonic crystal waveguides for e.g. telecommunication applications. The focus of the work was the loss measurement, coupling to strip waveguides and the dispersion properties of the photonic crystal waveguides. Silicon-on-insulator substrate was chosen as a material platform since it is suitable for applications at wavelengths above 1200 nm.

A novel method of characterization of short photonic crystal waveguides was developed in paper I. The method comprises patterning of Bragg mirrors patterned into the ends of the waveguide and analysing the Fabry-Pérot oscillations in the transmission spectra.

A new type of a photonic crystal, based on ring-shaped holes (RPhC), was introduced. The RPhC was used in the design of a dispersion tailored slow-light waveguide in paper III. An RPhCW coupler to efficiently inject light from a conventional strip waveguide into the slow mode was introduced in paper V. Fabrication and characterization of the RPhC waveguide in paper II is the first demonstration of the feasibility of the RPhC waveguide.

Slow modes exist in periodic waveguides because the forward and backward propagating modes are coupled due to periodicity. The group velocity depends on the phase match between these contradirectional modes, therefore the group velocity is usually highly wavelength dependent. The PhC waveguides can be designed in such a way that the interaction between the contradirectional modes depends on the frequency. Paper III showed that it is possible to tune the ring geometry of the RPhCW to compensate for the phase mismatch and thereby tailor the dispersion properties of the slow mode. The dispersion engineered slow-light RPhC waveguide has a group index of 55 ± 3 over a bandwidth of 5 nm at the wavelength 1.55 μm (loss minimum of the optical fiber).

Paper V and other recent studies show that slow modes in PhCWs can be efficiently coupled with strip waveguides with couplers having a length of just a few micrometers. The efficient coupling relies on evanescent Bloch modes that arise at the interface between two periodic waveguides. The analysis of the transmission spectra of the coupler with a dispersion tailored waveguide revealed that the coupling is not only a function of the group velocity difference, but it also depends on the phase

match between the modes in the two waveguides.

The slow-light PhC waveguides have favorable properties for implementation into photonic integrated circuits. They exhibit dispersion tailored slow modes, which are particularly interesting in telecommunications and signal processing applications. The compact and efficient couplers to the conventional strip waveguides are essential in the miniaturization task. Therefore PhC waveguides may enable realization of a hybrid photonic integrated circuit, where compact nonlinear slow-light devices are embedded into a photonic integrated circuit which can be based on e.g. strip waveguides for its main part. The slow-light device presented in Paper V exhibits an optical intensity enhancement by a factor of more than 10. This is a very promising result regarding the reduction of the footprint of photonic devices, in particular if nonlinear effects are involved.

It was shown in paper IV that the RPhC can be designed to enhance the interaction of the waveguide mode with the region outside the dielectric, which is favorable in e.g. biosensing. The same property may be interesting if the RPhC is covered with a material that has other peculiar optical properties. For example, an RPhC waveguide covered with a magnetic polymer could operate as a polarization converter.

References

[1] K. Kano, *Semiconductor devices* (Prentice-Hall, 1998).

[2] K. K. Lee, D. R. Lim, H.-C. Luan, A. Agarwal, J. Foresi and L. C. Kimerling, Applied Physics Letters **77**, 1617 (2000), URL http://link.aip.org/link/?APL/77/1617/1.

[3] M. Lipson, Lightwave Technology, Journal of **23**, 4222 (Dec. 2005), ISSN 0733-8724, URL http://dx.doi.org/10.1109/JLT.2005.858225.

[4] G. T. Reed, Nature **427**, 595 (2004), URL http://dx.doi.org/10.1038/427595b.

[5] T. Tsuchizawa, K. Yamada, H. Fukuda, T. Watanabe, J. ichi Takahashi, M. Takahashi, T. Shoji, E. Tamechika, S. Itabashi and H. Morita, Selected Topics in Quantum Electronics, IEEE Journal of **11**, 232 (Jan.-Feb. 2005), ISSN 1077-260X, URL http://dx.doi.org/10.1109/JSTQE.2004.841479.

[6] R. Soref and B. Bennett, Quantum Electronics, IEEE Journal of **23**, 123 (Jan 1987), ISSN 0018-9197, URL http://ieeexplore.ieee.org/xpl/tocresult.jsp?isnumber=23099.

[7] C. Barrios, V. Almeida, R. Panepucci and M. Lipson, Lightwave Technology, Journal of **21**, 2332 (Oct. 2003), ISSN 0733-8724, URL http://dx.doi.org/10.1109/JLT.2003.818167.

[8] A. Liu, R. Jones, L. Liao, D. Samara-Rubio, D. Rubin, O. Cohen, R. Nicolaescu and M. Paniccia, Nature **427**, 615 (2004), URL http://dx.doi.org/10.1038/nature02310.

[9] S. Manipatruni, Q. Xu and M. Lipson, Opt. Express **15**, 13035 (2007), URL http://www.opticsexpress.org/abstract.cfm?URI=oe-15-20-13035.

[10] Q. Xu, M. Lipson, B. Schmidt and S. Pradhan, Nature **435**, 325 (2005), URL http://dx.doi.org/10.1038/nature03569.

[11] M. A. Foster, A. C. Turner, M. Lipson and A. L. Gaeta, Opt. Express **16**, 1300 (2008), URL http://www.opticsexpress.org/abstract.cfm?URI=oe-16-2-1300.

[12] Q. Lin, O. J. Painter and G. P. Agrawal, Opt. Express **15**, 16604 (2007), URL http://www.opticsexpress.org/abstract.cfm?URI=oe-15-25-16604.

[13] H. Rong, A. Liu, R. Jones, O. Cohen, D. Hak, R. Nicolaescu, A. Fang and M. Paniccia, Nature **433**, 292 (2004), URL http://www.nature.com/nature/journal/v433/n7023/abs/nature03273.html.

[14] Y.-H. Kuo, H. Rong, V. Sih, S. Xu, M. Paniccia and O. Cohen, Opt. Express **14**, 11721 (2006), URL http://www.opticsexpress.org/abstract.cfm?URI=oe-14-24-11721.

[15] R. Salem, M. A. Foster, A. C. Turner, D. F. Geraghty, M. Lipson and A. L. Gaeta, Opt. Express **15**, 7802 (2007), URL http://www.opticsinfobase.org/abstract.cfm?URI=oe-15-12-7802.

[16] Q. Xu and M. Lipson, Opt. Express **15**, 924 (2007), URL http://www.opticsexpress.org/abstract.cfm?URI=oe-15-3-924.

[17] P. Dumon, W. Bogaerts, V. Wiaux, J. Wouters, S. Beckx, J. V. Campenhout, D. Taillaert, B. Luyssaert, P. Bienstman, D. V. Thourhout and R. Baets, Photonics Technology Letters, IEEE **16**, 1328 (May 2004), ISSN 1041-1135, URL http://dx.doi.org/10.1109/LPT.2004.826025.

[18] M. Settle, M. Salib, A. Michaeli and T. F. Krauss, Opt. Express **14**, 2440 (2007), URL http://www.opticsinfobase.org/abstract.cfm?URI=oe-14-6-2440.

[19] P. I. Borel, B. Bilenberg, L. H. Frandsen, T. Nielsen, J. Fage-Pedersen, A. V. Lavrinenko, J. S. Jensen, O. Sigmund and A. Kristensen, Opt. Express **15**, 1261 (2007), URL http://www.opticsexpress.org/abstract.cfm?URI=oe-15-3-1261.

[20] H. Benisty, C. Weisbuch, D. Labilloy, M. Rattier, C. Smith, T. Krauss, R. de la Rue, R. Houdre, U. Oesterle, C. Jouanin and D. Cassagne, Lightwave Technology, Journal of **17**, 2063 (Nov 1999), ISSN 0733-8724, URL http://dx.doi.org/10.1109/50.802996.

[21] H. Kosaka, T. Kawashima, A. Tomita, M. Notomi, T. Tamamura, T. Sato and S. Kawakami, Applied Physics Letters **74**, 1212 (1999), URL http://link.aip.org/link/?APL/74/1212/1.

[22] L. Wu, M. Mazilu and T. Krauss, Lightwave Technology, Journal of **21**, 561 (Feb. 2003), URL http://dx.doi.org/10.1109/JLT.2003.808773.

[23] H. Kosaka, T. Kawashima, A. Tomita, M. Notomi, T. Tamamura, T. Sato and S. Kawakami, Phys. Rev. B **58**, R10096 (1998), URL http://dx.doi.org/10.1103/PhysRevB.58.R10096.

[24] R. D. Meade, A. Devenyi, J. D. Joannopoulos, O. L. Alerhand, D. A. Smith and K. Kash, J. Appl. Phys. **75**, 4753 (1994), URL http://dx.doi.org/10.1063/1.355934.

[25] M. Notomi, A. Shinya, S. Mitsugi, E. Kuramochi and H.-Y. Ryu, Opt. Express **12**, 1551 (2004), URL http://www.opticsinfobase.org/abstract.cfm?URI=oe-12-8-1551.

[26] T. Niemi, L. Frandsen, K. Hede, A. Harpoth, P. Borel and M. Kristensen, Photonics Technology Letters, IEEE **18**, 226 (Jan. 1, 2006), ISSN 1041-1135, URL http://dx.doi.org/10.1109/LPT.2005.860001.

[27] A. Shinya, S. Mitsugi, E. Kuramochi and M. Notomi, Opt. Express **14**, 12394 (2006), URL http://www.opticsexpress.org/abstract.cfm?URI=oe-14-25-12394.

[28] H. Gersen, T. J. Karle, R. J. P. Engelen, W. Bogaerts, J. P. Korterik, N. F. van Hulst, T. F. Krauss and L. Kuipers, Physical Review Letters **94**, 073903 (pages 4) (2005), URL http://dx.doi.org/10.1103/PhysRevLett.94.073903.

[29] X. Letartre, C. Seassal, C. Grillet, P. Rojo-Romeo, P. Viktorovitch, M. L. V. d'Yerville, D. Cassagne and C. Jouanin, Applied Physics Letters **79**, 2312 (2001), URL http://dx.doi.org/10.1063/1.1405146.

[30] M. Notomi, K. Yamada, A. Shinya, J. Takahashi, C. Takahashi and I. Yokohama, Phys. Rev. Lett. **87**, 253902 (2001), URL http://dx.doi.org/10.1103/PhysRevLett.87.253902.

[31] A. Säynätjoki, M. Mulot, H. Lipsanen and J. Ahopelto, Opt. Express **15**, 8323 (2007), URL http://www.opticsinfobase.org/abstract.cfm?URI=oe-15-13-8323.

[32] Y. A. Vlasov, M. O'Boyle, H. F. Hamann and S. J. McNab, Nature **438**, 65 (2005), URL http://dx.doi.org/10.1038/nature04210.

[33] D. M. Beggs, T. P. White, L. O'Faolain and T. F. Krauss, Opt. Lett. **33**, 147 (2008), URL http://ol.osa.org/abstract.cfm?URI=ol-33-2-147.

[34] T. F. Krauss, Journal of Physics D: Applied Physics **40**, 2666 (2007), URL http://dx.doi.org/10.1088/0022-3727/40/9/S07.

[35] M. Roussey, M.-P. Bernal, N. Courjal, D. V. Labeke, F. I. Baida and R. Salut, Applied Physics Letters **89**, 241110 (pages 3) (2006), URL http://link.aip.org/link/?APL/89/241110/1.

[36] M. Soljačić and J. D. Joannopoulos, Nat Mater **3**, 211 (2004), URL http://dx.doi.org/10.1038/nmat1097.

[37] M. Soljačić, S. G. Johnson, S. Fan, M. Ibanescu, E. Ippen and J. D. Joannopoulos, J. Opt. Soc. Am. B **19**, 2052 (2002), URL http://josab.osa.org/abstract.cfm?URI=josab-19-9-2052.

[38] L. H. Frandsen, A. V. Lavrinenko, J. Fage-Pedersen and P. I. Borel, Opt. Express **14**, 9444 (2006), URL http://www.opticsinfobase.org/abstract.cfm?URI=oe-14-20-9444.

[39] A. Jafarpour, A. Adibi, Y. Xu and R. K. Lee, Phys. Rev. B **68**, 233102 (2003), URL http://dx.doi.org/10.1103/PhysRevB.68.233102.

[40] M. Settle, R. J. P. Engelen, M. Salib, A. Michaeli, L. Kuipers and T. F. Krauss, Opt. Express **15**, 219 (2007), URL http://www.opticsinfobase.org/abstract.cfm?URI=oe-15-1-219.

[41] J. P. Hugonin, P. Lalanne, T. P. White and T. F. Krauss, Opt. Lett. **32**, 2638 (2007), URL http://ol.osa.org/abstract.cfm?URI=ol-32-18-2638.

[42] N. Ozaki, Y. Kitagawa, Y. Takata, N. Ikeda, Y. Watanabe, A. Mizutani, Y. Sugimoto and K. Asakawa, Opt. Express **15**, 7974 (2007), URL http://www.opticsinfobase.org/abstract.cfm?URI=oe-15-13-7974.

[43] P. Pottier, M. Gnan and R. M. De La Rue, Opt. Express **15**, 6569 (2007), URL http://www.opticsinfobase.org/abstract.cfm?URI=oe-15-11-6569.

[44] L. Yang, A. Lavrinenko, L. Frandsen, P. Borel, A. Tetu and J. Fage-Pedersen, Electronics Letters **43**, 923 (August 16 2007), URL http://dx.doi.org/10.1049/el:20071509.

[45] K. Yee, Antennas and Propagation, IEEE Transactions on [legacy, pre - 1988] **14**, 302 (May 1966), ISSN 0096-1973, URL http://ieeexplore.ieee.org/search/srchabstract.jsp?arnumber=1138693&isnumber=2

[46] M. Qiu, *F2P software* (2001), URL http://www.imit.kth.se/info/FOFU/PC/F2P/.

[47] S. Johnson and J. D. Joannopoulos, Opt. Express **8**, 173 (2001), URL http://www.opticsinfobase.org/abstract.cfm?URI=oe-8-3-173.

[48] R. D. Meade, K. D. Brommer, A. M. Rappe and J. D. Joannopoulos, Phys. Rev. B **44**, 13772 (1991), URL http://dx.doi.org/10.1103/PhysRevB.44.13772.

[49] A. Yariv, *Optical Electronics in Modern Communications* (Oxford Univeristy Press, 1997).

[50] R. Kashyap, *Fiber Bragg Gratings* (Academic Press, 1999).

[51] M. Qiu, Phys. Rev. B **66**, 033103 (2002), URL http://dx.doi.org/10.1103/PhysRevB.66.033103.

[52] S. Assefa and Y. A. Vlasov, Opt. Express **15**, 17562 (2007), URL http://www.opticsexpress.org/abstract.cfm?URI=oe-15-26-17562.

[53] S. McNab, N. Moll and Y. Vlasov, Opt. Express **11**, 2927 (2003), URL http://www.opticsexpress.org/abstract.cfm?URI=oe-11-22-2927.

[54] G. P. Agrawal, *Fiber-Optic Communication Systems* (Wiley, 1997).

[55] S. Kubo, D. Mori and T. Baba, Opt. Lett. **32**, 2981 (2007), URL http://ol.osa.org/abstract.cfm?URI=ol-32-20-2981.

[56] K. Solehmainen, T. Aalto, J. Dekker, M. Kapulainen, M. Harjanne, K. Kukli, P. Heimala, K. Kolari and M. Leskela, Lightwave Technology, Journal of **23**, 3875 (Nov. 2005), ISSN 0733-8724, URL http://dx.doi.org/10.1109/JLT.2005.857750.

[57] J. S. Foresi, M. R. Black, A. M. Agarwal and L. C. Kimerling, Applied Physics Letters **68**, 2052 (1996), URL http://link.aip.org/link/?APL/68/2052/1.

[58] H. van de Stadt and J. M. Muller, J. Opt. Soc. Am. A **2**, 1363 (1985), URL http://josaa.osa.org/abstract.cfm?URI=josaa-2-8-1363.

[59] S. Olivier, M. Rattier, H. Benisty, C. Weisbuch, C. J. M. Smith, R. M. De La Rue, T. F. Krauss, U. Oesterle and R. Houdré, Phys. Rev. B **63**, 113311 (2001), URL http://dx.doi.org/10.1103/PhysRevB.63.113311.

[60] H. Benisty, D. Labilloy, C. Weisbuch, C. J. M. Smith, T. F. Krauss, D. Cassagne, A. Béraud and C. Jouanin, Applied Physics Letters **76**, 532 (2000), URL http://dx.doi.org/10.1063/1.125809.

[61] R. Engelen, Y. Sugimoto, Y. Watanabe, J. Korterik, N. Ikeda, N. van Hulst, K. Asakawa and L. Kuipers, Opt. Express **14**, 1658 (2006), URL http://www.opticsexpress.org/abstract.cfm?URI=oe-14-4-1658.

[62] Y. A. Vlasov and S. J. McNab, Opt. Lett. **31**, 50 (2006), URL http://ol.osa.org/abstract.cfm?URI=ol-31-1-50.

[63] C. M. de Sterke, J. Walker, K. B. Dossou and L. C. Botten, Opt. Express **15**, 10984 (2007), URL http://www.opticsexpress.org/abstract.cfm?URI=oe-15-17-10984.

[64] H. Kurt and D. S. Citrin, Opt. Express **13**, 10316 (2005), URL http://www.opticsinfobase.org/abstract.cfm?URI=oe-13-25-10316.

[65] N. Skivesen, A. Tétu, M. Kristensen, J. Kjems, L. H. Frandsen and P. I. Borel, Opt. Express **15**, 3169 (2007), URL http://www.opticsinfobase.org/abstract.cfm?URI=oe-15-6-3169.

[66] S. Hughes, L. Ramunno, J. F. Young and J. E. Sipe, Physical Review Letters **94**, 033903 (pages 4) (2005), URL http://link.aps.org/abstract/PRL/v94/e033903.

ISBN 978-951-22-9383-4
ISBN 978-951-22-9384-1 (PDF)
ISSN 1795-2239
ISSN 1795-4584 (PDF)